Importance of ice elasticity in simulating tide-induced grounding line variations along prograde bed slopes

Natalya Ross[1], Pietro Milillo[1,2,3], Kalyana Nakshatrala[1], Roberto Ballarini[1], Aaron Stubblefield[4], Luigi Dini[5]

[1]Department of Civil & Environmental Engineering, University of Houston, Houston, TX, USA
[2]Department of Earth and Atmospheric Sciences, University of Houston, Houston, TX, USA
[3]German Aerospace Center (DLR), Microwaves and Radar Institute, Munich, Germany
[4]Earth System Science Interdisciplinary Center, University of Maryland, College Park, MD, USA
[5]Italian Space Agency (ASI), Matera, Italy

Correspondence to: Natalya Ross (nmaslenn@cougarnet.uh.edu)

Abstract. The grounding line, delineating the boundary where a grounded glacier becomes afloat in ocean water, shifts in response to tidal cycles. Here, we analyze COSMO-SkyMed Differential Interferometric Synthetic Aperture Radar (DInSAR) data acquired in 2020 and 2021 over Totten, Moscow University, and Rennick glaciers in East Antarctica, detecting tide-induced grounding line position variations from 0.5 to 12.5 km along prograde slopes ranging from ~0 to 5%. Considering a glacier as a non-Newtonian fluid, we provide two-dimensional formulations of viscous and viscoelastic short-term behavior of a glacier while in partial frictional contact with the bedrock, and partially floating on seawater. Since the models' equations are not amenable to analytical treatment, numerical solutions are obtained using FEniCS, an open-source Python package for solving partial differential equations using the finite element method. We establish the dependence of the grounding zone width on glacier thickness, bed slope, and glacier flow speed. The predictions of the viscoelastic model match ~97% of all the DInSAR grounding zone measurements and are ∼74% more accurate than those of the purely viscous model. This study underscores the critical role played by ice elasticity in continuum mechanics-based glacier models and demonstrates how these models can be validated using DInSAR measurements.

1. Introduction

The grounding line, which delineates the transition between the bedrock-based ice sheet and the floating ice shelf, is crucial for Antarctic research (Friedl et al., 2020; Haseloff and Sergienko, 2018). This boundary is a fundamental indicator of glacier stability, as its position reflects the glacier dynamics and influences the overall glacier force and mass balances (Davison et al., 2023; Holland, 2008). Grounding lines not only provide valuable information about glacier stability by enabling the evaluation of ice thickness, but also allow for the monitoring of sea level changes due to climate change (Goldstein et al., 1993; Schoof, 2007). Mechanisms governing variations in grounding line position are complex and involve both long-term and short-term processes (Sergienko and Haseloff, 2023; Sergienko, 2022). Short-term grounding line migrations are induced by tidal forces and occur within a tidal cycle (Albrecht et al., 2006; Coleman et al., 2002), while long-term migrations depend primarily on changes in ice dynamics and climate (Freer et al., 2023; Lowry et al., 2024). Models of grounding line evolution over time scales significantly exceeding tidal scales neglect short-term variations (Cornford et al., 2020; Gagliardini et al., 2016; Seroussi et al., 2014). Conversely, short-term glacier models focus on tidal time scales and tend to disregard the long-term evolution of glaciers due to its

negligible impact over these shorter periods (Rosier et al., 2014; Rosier and Gudmundsson, 2020). Here, we focus on short-term, tide-induced grounding line migrations, which can extend up to several kilometers (Brancato et al., 2020; Brunt et al., 2010; Dawson and Bamber, 2017; Milillo et al., 2022; Minchew et al., 2017).

Several short-term glacier dynamics models, employing various physical approaches, have been developed to interpret tide-induced migrations. For example, a hydrological model proposed by Warburton et al. (2020) defines the grounding zone width as the penetration depth into a subglacial cavity of water interacting with an elastic ice beam that responds to ocean tides. Sayag and Worster (2011, 2013) describe grounding line migration as the result of tidal force-induced deformation of an elastic Euler-Bernoulli beam, which moves vertically in response to the periodic tidal forces. Tsai and Gudmundsson (2015) consider a grounding zone as an opening and closing of a crack between an elastic ice beam and the bedrock, using equations governing the propagation of a water-filled crack under pressure. This model (Tsai and Gudmundsson, 2015), which cannot predict grounding line migrations at low tides, was modified and applied to the Amery Ice Shelf in Antarctica by Chen et al. (2023), who showed that a crack model can reproduce a kilometer grounding line retreat over a tidal cycle. Nevertheless, the crack-based method is one-dimensional, as it considers only the glacier motion along the ice-bedrock surface without describing motion-induced changes within the ice.

Other previously proposed short-term models treat glacier ice as a viscous or viscoelastic fluid, aiming to determine grounding line migration by resolving contact forces at the base (Stubblefield et al., 2021). Rosier et al. (2014) and Rosier and Gudmundsson (2020) developed nonlinear viscoelastic models on tidal time scales, where normal stress and velocity determine the grounding line position. However, being considered after discretization, these factors are not incorporated into the variational formulation. This technical detail was addressed by Stubblefield et al. (2021), who used the full Navier-Stokes equations for purely viscous flow and included contact conditions in the variational formulation. However, Stubblefield et al. (2021) did not compare the outputs of the viscous model with grounding zone width measurements. Here, we extend the viscous model proposed by Stubblefied et al. (2021) by incorporating an elastic component within the framework of the upper-convected Maxwell model (Gudmundsson, 2011; Snoeijer et al., 2020). The model formulation utilizes variational inequalities derived from the governing equations using boundary conditions on ice velocity and normal stress. The variational inequalities are transformed into variational equalities via a penalty method. Grounding line migrations are calculated by solving these variational equations at each time step using the Finite Element Method (FEM) in the open-source FEniCS package (Alnæs et al., 2015; Logg et al., 2012). Glacier thickness, bedrock slope, and ice flow serve as model inputs, and are set based on BedMachine Antarctica (Morlighem et al., 2017) and MEaSUREs InSAR-based ice velocity map of Antarctica (Rignot et al., 2017). We compare model results with grounding zone width measurements from Cosmo-SkyMed Differential Interferometric Synthetic Aperture Radar (DInSAR) data acquired between 2020 and 2021 over East Antarctica. Specifically, we focus on Totten (TOT), Moscow University (MU), and Rennick (REN) glaciers, which are characterized by kilometric tide-induced grounding line migrations. Comparing modelled and DInSAR-based grounding zones, we evaluate both models' performance and assess the significance of the elastic component relative to the formulation that accounts for only viscosity. Additionally, we determine the impact of the ice-bed system's main

parameters, namely, bedrock slope, glacier thickness, and ice velocity, on the magnitude of tidally induced grounding line migrations.

2. Data and methods

2.1. Study area

This study focuses on three glaciers, MU, TOT, and REN, whose relative locations in Antarctica are shown in Figure 1. MU and TOT are neighboring glaciers, located on the Sabrina Coast in East Antarctica (Bensi et al., 2022; Fernandez et al., 2018; Orsi and Webb, 2022). Together, the combined effect of these two glaciers may result in up to a 5-meter sea level rise, making them major contributors to sea level changes in East Antarctica (Mohajerani et al., 2018). Being characterized by the highest outflow and thinning rate in East Antarctica, TOT also has the third-largest ice flux among all Antarctic glaciers, following Pine Island and Thwaites glaciers (Pritchard et al., 2009; Rignot and Thomas, 2002; Roberts et al., 2018). In contrast, MU exhibits relatively slow thinning rates (Mohajerani et al., 2018) and nearly half the basal melt rate of TOT: 4.7 ± 0.8 m/yr vs 10.5 ± 0.7 m/yr between 2003 and 2008, respectively (Rignot et al., 2013). Both glaciers are grounded below the sea level, making them potentially unstable and susceptible to collapse (Van Achter et al., 2022; Aitken et al., 2016).

REN, situated in Northern Victoria Land in East Antarctica, spans over 400 km along the flow and narrows from 80 km to 25 km across the flow (Allen et al., 1985; Mayewski et al., 1979; Meneghel et al., 1999; Sturm and Carryer, 1970). Containing the sea-level equivalent of 11 cm in the form of ice, REN is also grounded below the sea level and is experiencing rapid thinning due to intensive basal melt (Pritchard et al., 2012; Rignot et al., 2019). REN's ice discharge has shown up to 20% amplification between 1999 and 2018 (Miles et al., 2022). Although REN behaves similarly to TOT and MU, it retreats slower than most Antarctic glaciers, rendering it relatively stable (Miles et al., 2022; Pritchard et al., 2012).

2.2. Glacier parameters used as model inputs

Since the model requires glacier thickness, bed slopes, and ice speed as input parameters, we estimated these values for the three glaciers of interest. To achieve this, we determined 69 profile lines: 33 lines over MU, 17 over TOT, and 19 over REN (Figure 1).

2.2.1. SAR-based ice flow velocities

The profiles were oriented in the direction of ice flow, derived from the SAR-based ice velocity map of Antarctica (Rignot et al., 2017), provided by NASA's MEaSUREs program. This dataset includes the v_x and v_y components of the ice velocities $\boldsymbol{v}$ in m / year, projected to EPSG3031 at 450 m resolution. The direction of the ice flow was calculated as $\arctan(v_y/v_x)$ in degrees and shown with black arrows in Figure 1. Flow lines were selected along the flow direction and were spaced 500 to 600 m apart. Each profile is approximately 20 km long, as this length was adopted as the glacier domain length for the modeling process. The flow lines, and consequently the selected profiles, are not always parallel to the grounding lines, indicating the influence of crossflow heterogeneity in our analysis. To estimate the flow speed, we calculated the magnitude of the ice flow vectors (or the velocity map) as $\sqrt{v_x^2 + v_y^2}$,

106   extracted the values from the velocity map along the profile lines, and computed the average ice flow for each profile.

107   The summary of the calculated ice flow velocities along the selected 69 profiles is provided in Table S1.

108
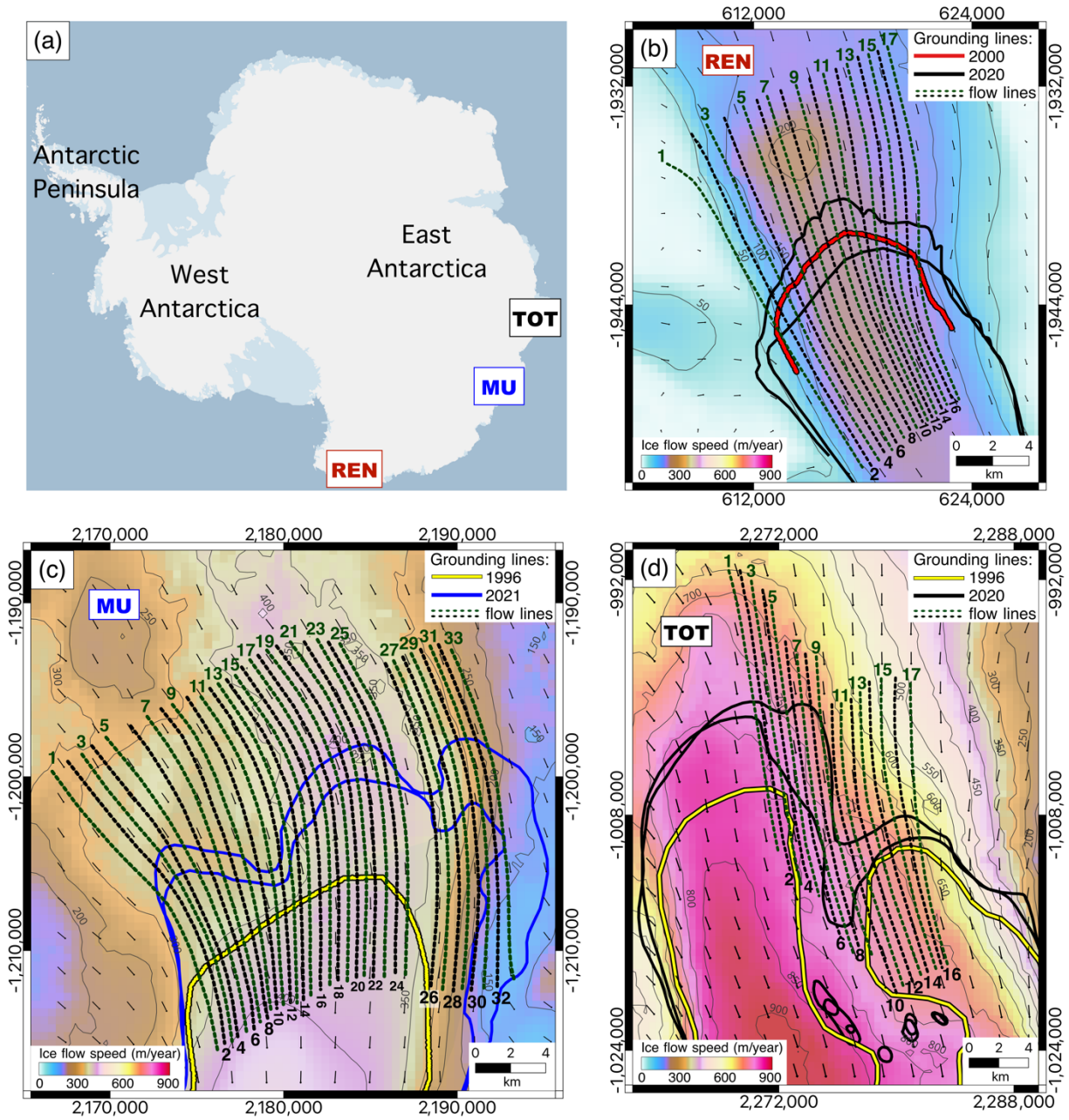
109   **Figure 1.** Study area: (a) location of TOT, MU, and REN in Antarctica; and ice velocity map over b) REN, c) MU,

110   d) TOT. The selected 69 profiles are shown as dashed green and black lines over the black ice flow vectors, derived

111   from the MEaSUREs InSAR-based ice velocity map of Antarctica (Rignot et al., 2017). For visualization purposes,

112   the flow vectors shown here were calculated over a velocity flow map resampled at 2 km, while the directions of the

113   profiles were determined over the original 450 m resolution flow map to maximize the accuracy of the flow direction

114   definition. The grounding lines over REN and TOT were mapped in 2020 (black line), while the grounding lines over

115   MU (blue line) correspond to 2021. The grounding lines for 1996 (yellow line) and 2000 (red line) were taken from

116 MEaSUREs2 DInSAR-based Antarctic grounding line dataset (Rignot et al., 2016). All maps are represented in
117 Antarctic projection (EPSG:3031).

2.2.2. Ice thickness and bed slope

119 Glacier thickness values were determined using the 500 m-resolution ice thickness map from BedMachine Antarctica
120 (version 2) (Morlighem et al., 2017), as shown in Figure 2. Thickness values were extracted along the profiles, and
121 the average thickness was calculated for each profile. Bed slopes for each profile were determined using the 500 m-
122 resolution BedMachine Antarctica topographic map (Figure 2) by linearly approximating extracted bed elevation
123 values and calculating the slope of the fitted line. The summary of the calculated glacier thicknesses and bed slopes
124 along the selected 69 profiles is provided in Table S1.
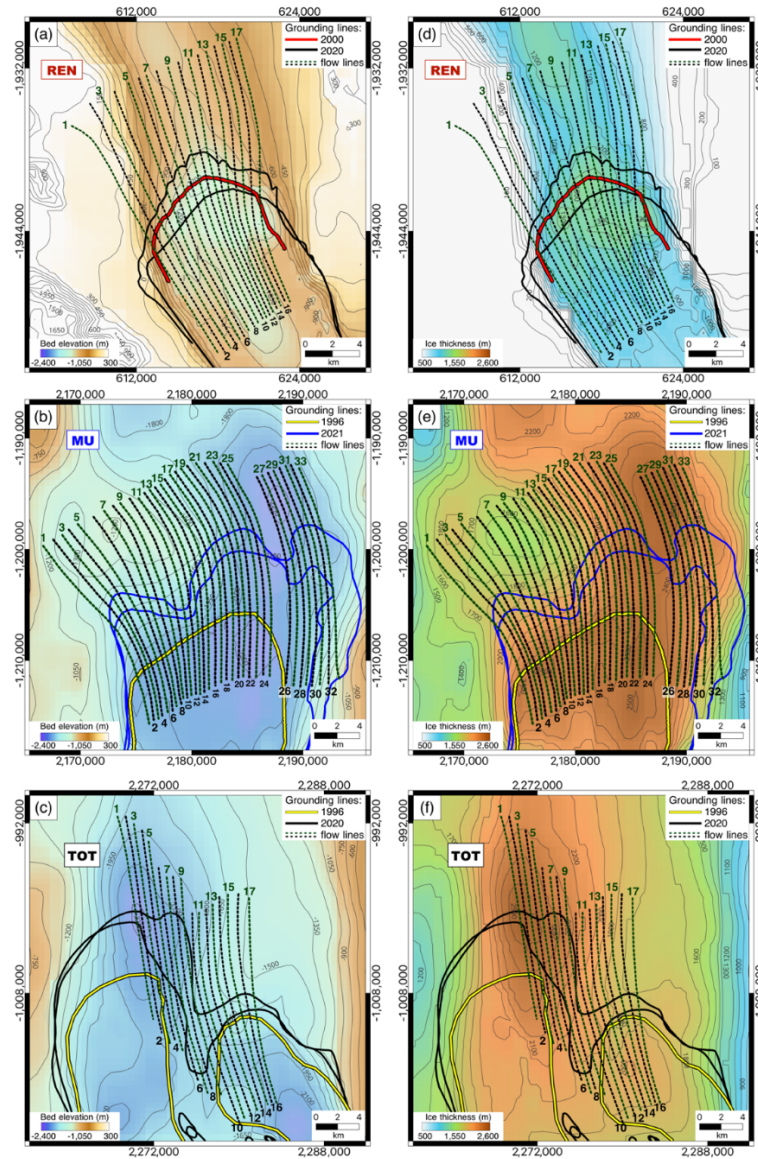
125
126 **Figure 2.** Bed elevation relief from BedMachine2 (Morlighem et al., 2017) over a) REN, b) MU, c) TOT; and ice
127 thickness maps from BedMachine2 (Morlighem et al., 2017) over d) REN, e) MU, and f) TOT. The selected 69 profiles

128   are shown as dashed green and black lines. The grounding lines over REN and TOT were mapped in 2020 (black line),

129   while the grounding lines over MU (blue line) correspond to 2021. The grounding lines for 1996 (yellow line) and

130   2000 (red line) were taken from MEaSUREs2 DInSAR-based Antarctic grounding line dataset (Rignot et al., 2016).

131   All maps are represented in Antarctic projection (EPSG:3031).

2.2.3. DInSAR-based grounding widths for model validation

133   As the model estimates grounding zone values, grounding zone measurements are required to assess the model

134   performance. We obtained the grounding zone width values for TOT, MU, and REN by utilizing a series of 1-day

135   repeat pass Synthetic Aperture Radar (SAR) data from the COSMO-SkyMed (CSK) mission, operated by the Italian

136   Space Agency (ASI). The first generation of the mission comprises a constellation of four satellites equipped with

137   synthetic aperture radars operating at X-band with a wavelength of 3.1 cm (Milillo et al., 2014). Each of the four first-

138   generation satellites has a 16-day repeat cycle, while the second and third satellites capture InSAR data over the same

139   area with a 1-day interval. Interferograms were generated using GAMMA software (Werner et al., 2000) from CSK

140   STRIPMAP data, following a validated processing chain (Brancato et al., 2020; Milillo et al., 2017). Satellite

141   acquisitions were designed as a set of five consecutive overlaying 40×40 km swath frames with an azimuth and range

142   resolution of 3 meters. To eliminate topographic effects, the Copernicus digital elevation model (DEM) is employed.

143   To co-register the data and achieve maximum phase coherence, we used satellite orbits for coarse co-registration and

144   used a pixel offsets approach for fine co-registration. A multi-looking factor of 10 in both range and azimuth was used

145   to achieve an interferogram resolution of 30 m x 30 m. Two one-day interferometric pairs were combined into one

146   double differential interferogram (DInSAR) to cancel out horizontal deformation due to glacier flow. Each

147   interferometric pair combined in a double difference DInSAR interferogram is acquired within 1.5 months over the

148   same satellite track to minimize horizontal velocity changes and highlight vertical glacier motion, enabling grounding

149   line mapping (Milillo et al., 2022). Double difference DInSAR interferograms from different orbits acquired at

150   different times ensured sensitivity to several frequencies of the tidal spectrum (Milillo et al 2017, Minchew et al 2017).

151   An interferometric fringe corresponds to half a wavelength of surface displacement, equivalent to 1.5 cm of satellite

152   line of sight displacement per fringe for X-band or about 1.7 cm when projecting deformation onto the vertical

153   considering the satellite incidence angle. The grounding line can be manually delineated as the most inner fringe in

154   the grounded ice side. Therefore, the DInSAR technique provides information about vertical tide-induced glacier

155   movements and enables manual grounding line mapping with an average empirically determined manual mapping

156   accuracy of 100 - 200 m (Rignot et al., 2014; Ross et al., 2024). To connect the models with the observations, we

157   needed to link every SAR image to its unique sea level and atmospheric pressure level, which also introduced vertical

158   displacement due to the inverse barometer effect (IBE) (Padman et al., 2002). The IBE correction was performed by

159   examining anomalies in mean sea level pressure, reconstructed using the fifth generation of the European Centre for

160   Medium-Range Weather Forecasts (ECMWF) atmospheric reanalysis dataset of the global climate (ERA-5; Table S6)

161   (Hersbach et al., 2020). The tidal heights during the acquisition of the SAR images were determined using the Circum-

162   Antarctic Tidal Simulation (CATS2008) model (Padman et al., 2002) and listed in Table S6. Despite that one double

163   difference DInSAR interferogram is a combination of four SAR images, characterized by four different sea levels,

164   one DInSAR interferogram provided only one grounding line measurement. A high tide lifts the glacier, allowing

seawater to penetrate under the glacier, while a low tide causes the glacier to readvance. Following Milillo et al. (2022), we assumed that the grounding line position observed in a DInSAR interferogram corresponds to the largest combination of tidal level and IBE among the four SAR acquisitions. To estimate the grounding zone width for one glacier, we used a pair of double difference DInSAR interferograms. A maximum acquisition gap of 1.5 months between the interferograms in a pair ensures that any variations in the grounding line position occurs due to the tidal interaction rather than glacier retreat (Milillo et al., 2022). The difference between the largest IBE-corrected tidal heights (Column H in Table S6) in each pair of DInSAR interferograms is 0.95 m for MU, 1.03 m for TOT, and 1.08 m for REN (Column ΔH in Table S6). For each pair of interferograms, the interferogram with the higher H value represents the inland position of the grounding line and corresponds to the ocean tide, referred to as 'high tide' in the model. Conversely, the interferogram with the lower H value represents the outward position of the grounding line, corresponding to 'low tide' in the model. To ensure a valid comparison between the DInSAR-derived grounding zones and the modeled grounding zones, the IBE-corrected tidal levels listed in column H of Table S6 are used to evaluate the grounding zone width in the model. We measure the modeled grounding zone widths by calculating the difference between the grounding line position at maximum H and at minimum H.

Combining two manually mapped grounding lines for each interferogram in a pair, we established a grounding zone for the corresponding glacier and measure the grounding zone widths along the selected profiles. Therefore, one pair of DInSAR interferograms for MU, allowed us to obtain 33 grounding zone width values, as 33 profiles were originally selected over this glacier. Analogously, we obtained 19 grounding zone widths for REN, and 17 for TOT. Taking the higher limit of the grounding line mapping error of 200 m (Rignot et al., 2014; Ross et al., 2024), we determined the largest level of uncertainty of 400 m for each grounding zone measurement due to error propagation (see measurements error bars in Figure 6 (c)). The summary of the grounding zone width measurements is provided in Table S1, the grounding zone width measurement process for MU, TOT, and REN is visualized in Figure 3, which shows all three pairs of DInSAR interferograms, corresponding to low and high tide, and the 69 profiles along which the grounding zone width measurements were performed.

189
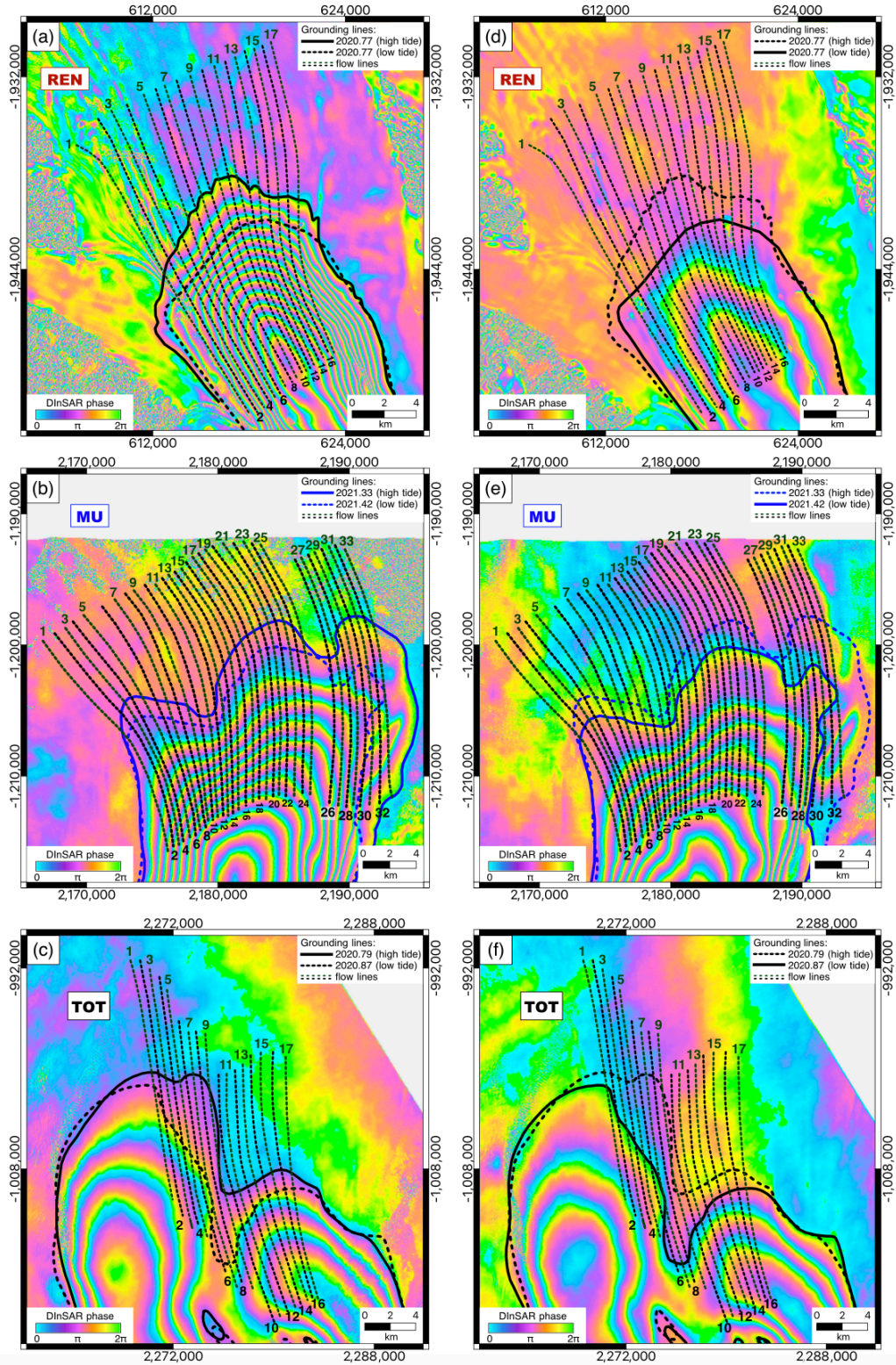
Figure 3. Pairs of DInSAR interferograms over a) REN, b) MU, c) TOT at high tide, and over d) REN, e) MU, f) TOT at low tide with corresponding manually mapped grounding lines. All interferograms are represented in Antarctic projection (EPSG:3031).

3. Viscous and viscoelastic models

The short-term grounding line migration model, rooted in the Navier-Stokes equations under the assumption of viscoelastic ice flow, builds upon the purely viscous formulation of the same problem (Stubblefield et al., 2021). Here, we provide the comprehensive description of the viscoelastic model along with a comparison between the viscous and viscoelastic models.

3.1. Principal notation

The notation used in the paper is listed in Table 1 and is further explained during the model formulation. In addition to summarizing the quantities and their corresponding mathematical symbols, Table 1 also provides the units and identifies the field type to which each quantity belongs, such as scalar, vector, or tensor field.

Table 1. Models′ principal notation.

Symbol	Quantity	Field type	Units
Geometry-related quantities			
(X, Y)	laboratory coordinate system	2D coordinate system	(m, m)
$x = (x, y)$	spatial point x with coordinates x and y	Point in 2D space	(m, m)
Ω	2D glacier domain	2D spatial domain	(m, m)
$\partial\Omega$	boundary of the glacier domain	Geometric boundary	m
Γ_D	inflow boundary	Geometric boundary	m
Γ_N	outflow boundary	Geometric boundary	m
Γ_a	ice–air surface	Geometric boundary	m
Γ_b	ice–bedrock surface	Geometric boundary	m
Γ_w	ice–water surface	Geometric boundary	m
Γ_s	lower glacier boundary	Geometric boundary	m
$h(x, t)$	surface elevation of the ice shelf	Scalar	m
$s(x, t)$	lower boundary of the ice shelf	Scalar	m
α	bedrock slope	Scalar	$\%$
$b(x)$	bedrock slope function	Scalar	m
A	bedrock inclination parameter	Scalar	m
L	glacier length	Scalar	m
$H(t)$	glacier thickness	Scalar	m
$l(t)$	sea level	Scalar	m
$\hat{n}(x)$	unit outward normal vector at point x of a domain boundary	Vector	$-$
Materials properties			
ρ_i	ice density	Scalar	$kg \cdot m^{-3}$
ρ_w	water density	Scalar	$kg \cdot m^{-3}$
ϕ	friction	Scalar	$Pa \cdot s \cdot m^{-1}$
C	friction coefficient	Scalar	$Pa \cdot \left(\frac{s}{m}\right)^{\frac{1}{n}}$
η	ice viscosity	Scalar	$Pa \cdot s$
G	shear modulus	Scalar	Pa
λ	relaxation time	Scalar	s

n	stress exponent (from the Glen's flow law)	Scalar	$-$
A	ice softness	Scalar	$Pa^{-n} \cdot s^{-1}$
Physical quantities			
t	time	Scalar	s
p	ice pressure	Scalar	Pa
p_w	water pressure at the ice–water interface	Scalar	Pa
p_w^0	hydrostatic water pressure	Scalar	Pa
v_0	inflow speed on Γ_D	Scalar	$m \cdot s^{-1}$
v	ice flow velocity	Vector	$m \cdot s^{-1}$
g	acceleration due to gravity	Vector	$m \cdot s^{-2}$
D	strain rate tensor	Tensor	s^{-1}
T	Cauchy stress tensor	Tensor	Pa
τ	deviatoric stress tensor	Tensor	Pa
Mathematical operators			
$\mathbb{I}$	identity tensor	Tensor	$-$
$\mathbb{P}$	orthogonal projection onto the boundary	Tensor	$-$
∇	spatial gradient operator	Operator	m^{-1}
$\nabla \cdot$	spatial divergence operator	Operator	m^{-1}
$\cdot$	inner (dot) product	Operator	$-$
$\otimes$	tensor product	Operator	$-$
$\overset{\triangledown}{\tau}$	upper-convected time derivative of some tensor field (in this case, of the tensor τ)	Operator	$Pa \cdot s^{-1}$
Model numerical parameters			
$\delta \ll 1$	Glen's flow law numerical parameter, used to prevent model numerical instabilities	Scalar	s^{-2}
$\varepsilon \ll 1$	Numerical parameter in the friction expression, used to prevent numerical instabilities	Scalar	$m^2 \cdot s^{-2}$

3.2. Glacier domain

For both models, we designate the glacier domain as Ω, as shown in Figure 4, with a piecewise smooth boundary $\partial\Omega$. We place the glacier in a two-dimensional coordinate system (X, Y), where X denotes the horizontal axis, and Y is used for identifying the vertical axis. In the principal notation used in this paper, a spatial point is denoted by $x = (x, y) \in \bar{\Omega}$, where an overline denotes the set closure. For glacier length L, the ice domain Ω can be mathematically expressed as

$$\Omega = \left\{ (x, y): \ |x| < \frac{L}{2}, \ \ s(x, t) < y < h(x, t) \right\} \tag{1}$$

The glacier boundary is represented as a union of five complementary parts:

$$\partial\Omega = \Gamma_D \cup \Gamma_N \cup \Gamma_w \cup \Gamma_b \cup \Gamma_a, \tag{2}$$

where Γ_D is an inflow boundary, Γ_N is an outflow boundary, Γ_w is an ice–water surface, Γ_b is an ice–bedrock surface, and Γ_a is an ice–air surface. Defining $f(x)$ as a bedrock slope function, $h(x, t)$ as a time-dependent function of the glacier surface elevation, and $s(x, t)$ as a function, defining the position of lower boundary of the ice shelf with time, the ice–water and ice–bed boundaries are expressed as

$$\Gamma_w = \{(x, y) \in \partial\Omega : y = s(x, t) > f(x)\}, \tag{3}$$

$$\Gamma_b = \{(x, y) \in \partial\Omega : y = s(x, t) = f(x)\}. \tag{4}$$

214 The entire lower boundary Γ_s therefore, is identified as a union of the ice–water and ice–bed boundaries:

$$\Gamma_s = \Gamma_w \cup \Gamma_b = \{(x, y) \in \partial\Omega : y = s(x, t) \geq f(x)\} \tag{5}$$

215 The grounding line position is the point where the ice–water boundary intersects the ice–bed boundary.

216
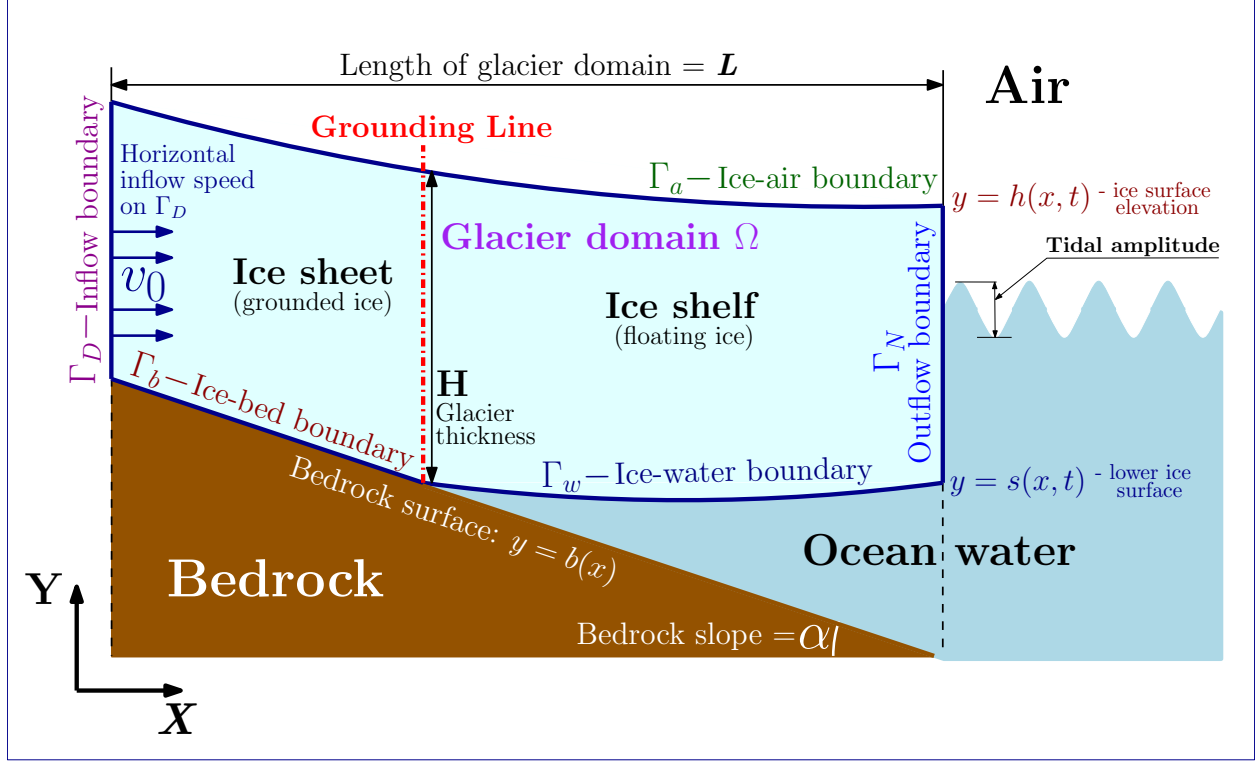
Figure 4. Model geometry for both viscous and viscoelastic problems, highlighting the ice domain Ω boundaries, as
defined in Table 1.

3.3. Model formulation

220 Here, we describe the formulation of both models, which have the same domain and boundary conditions, but different
221 governing equations. The summary of the notation mentioned here is provided in Table 1.

3.3.1. Governing equations

223 In both models, a glacier behaves as an incompressible non-Newtonian fluid, either viscous or viscoelastic.
224 Incompressibility means that the fluid density does not change during flow, which mathematically implies zero
225 divergence of the flow velocity $\boldsymbol{v}$:

$$\nabla \cdot \boldsymbol{v} = 0. \tag{6}$$

226 Both models are described by Cauchy's first law of motion under quasi-static conditions, which provides the
227 momentum conservation, expressed as:

$$\nabla \cdot \boldsymbol{T}(\boldsymbol{v}, p) + \rho_i \boldsymbol{g} = 0, \tag{7}$$

228 where T is the Cauchy stress tensor, ρ_i is the ice density, and $\boldsymbol{g}$ is the gravitational acceleration vector, which in the

229 glacier reference system is identified as $\boldsymbol{g} = g(0 \quad -1)^T$ with magnitude g.

230 The difference between the models becomes apparent when considering the constitutive law, which defines the

231 physical nature of the models. The viscous model is described by the following equation:

$$T(\boldsymbol{v}, p) = -p\mathbb{I} + 2\eta(\boldsymbol{v})\boldsymbol{D}, \tag{8}$$

232 where p is the ice pressure, $\mathbb{I}$ is a second-order identity tensor, $\eta(\boldsymbol{v})$ is a velocity-dependent ice viscosity, and $\boldsymbol{D}$ is a

233 strain rate tensor

$$\boldsymbol{D}(\boldsymbol{v}) = \frac{1}{2}[\nabla\boldsymbol{v} + (\nabla\boldsymbol{v})^T]. \tag{9}$$

234 Ice viscosity in the viscous model is identified via Glen's flow as

$$\eta(\boldsymbol{v}) = 2^{\frac{-1-n}{2n}} \cdot \sqrt[-n]{A}(|\boldsymbol{D}(\boldsymbol{v})|^2 + \delta)^{\frac{1-n}{2n}}, \tag{10}$$

235 where $n \geq 1$ is the stress exponent, $A > 0$ is the ice softness, and $\delta \ll 1$ is an infinitesimal numerical parameter, used

236 to prevent numerical instability of the models at zero strain rate.

237 For the viscoelastic model, constitutive law (8) and the viscosity expression (10) are principally different. We consider

238 the Maxwell model of viscoelasticity, which considers both viscous and elastic components. The Maxwell model

239 assumes that deformation properties can be represented by a purely elastic spring and a purely viscous dashpot

240 connected in series. Therefore, in the Maxwell model, a viscoelastic material behaves as a purely viscous flow under

241 slow deformation (long timescale), while it exhibits elastic resistance to rapid deformations (short timescale).

242 However, since the simple Maxwell model describes small deformations, we apply the upper-convected Maxwell

243 model, which includes some geometrical non-linearity. The constitutive relation for the viscoelastic model is identified

244 as

$$T(\boldsymbol{v}, p) = -p\mathbb{I} + \boldsymbol{\tau}, \tag{11}$$

245 where, compared to the purely viscous model (8), the strain rate tensor $\boldsymbol{D}$ (equation (9)) is replaced with the deviatoric

246 stress tensor $\boldsymbol{\tau}$, which is strain rate-dependent:

$$\boldsymbol{\tau} + \lambda\overset{\triangledown}{\boldsymbol{\tau}} - 2\eta(\boldsymbol{\tau})\boldsymbol{D}(\boldsymbol{v}) = 0, \tag{12}$$

247 where $\lambda = \frac{\eta(\boldsymbol{\tau})}{G}$ is the relaxation time with the shear modulus G. The viscoelastic model reduces to the viscous model

248 described in Stubblefield et al. (2021) when $\lambda = 0$, while at infinitely big λ, the upper-convected Maxwell model

249 reduces to a neo-Hookean elastic solid (Snoeijer et al., 2020). The ice viscosity in equation (12) is

$$\eta(\boldsymbol{\tau}) = \frac{1}{2A|\boldsymbol{\tau}|^{n-1}}. \tag{13}$$

250 $\overset{\triangledown}{\boldsymbol{\tau}}$ represents the upper-convected time derivative of $\boldsymbol{\tau}$:

$$\overset{\triangledown}{\boldsymbol{\tau}} = \frac{D\boldsymbol{\tau}}{Dt} - (\nabla\boldsymbol{v})^T \cdot \boldsymbol{\tau} - \boldsymbol{\tau} \cdot \nabla\boldsymbol{v}, \tag{14}$$

251 where $\frac{D\boldsymbol{\tau}}{Dt} = \frac{\partial\boldsymbol{\tau}}{\partial t} + \boldsymbol{v} \cdot \nabla\boldsymbol{\tau}$ is the material derivative of $\boldsymbol{\tau}$. The partial time derivative of $\boldsymbol{\tau}$ on the current time step is

252 calculated using the value from the previous time step, applying the backward Euler approximation:

$$\frac{\partial \boldsymbol{\tau}(x,t)}{\partial t} = \frac{\boldsymbol{\tau}(x,t) - \boldsymbol{\tau}(x,t - \Delta t)}{\Delta t}. \tag{15}$$

3.3.2. Evolution of the lower boundary

The time evolution of the lower boundary $y = s(x,t)$ is governed by the kinematic equation, which states that the surface moves with the ice flow. Assuming no mass changes at the lower surface, such as melting or freezing, the equation can be written as (Hirt and Nichols, 1981; Schoof, 2011):

$$\frac{\partial s}{\partial t} + v_x \frac{\partial s}{\partial t} = v_y, \tag{16}$$

where v_x and v_y are the components of the surface velocity vector $\boldsymbol{v}|_s = \left(v_x, v_y\right)^T$. Rewriting equation (16) in terms of the outward-pointing normal to the lower boundary $\widehat{\boldsymbol{n}}|_s = \frac{\left(\frac{\partial s}{\partial x}, \ -1\right)^T}{\sqrt{1 + \left(\frac{\partial s}{\partial x}\right)^2}}$, we get

$$\frac{\partial s}{\partial t} = -\boldsymbol{v} \cdot \widehat{\boldsymbol{n}}|_s \cdot \sqrt{1 + \left(\frac{\partial s}{\partial x}\right)^2}. \tag{17}$$

Since the solution of equation (17) is numerically unstable (Durand et al., 2009), we apply the backward Euler method to remove the instability. Denoting the approximate solution on k-th time step as s_*, such as $s_* \equiv s(x, t_k)$, and applying the backward Euler method to equation (17) under the assumption that $\left(\frac{\partial s}{\partial x}\right)^2 \ll 1$, we get

$$s_*(x, t_k) = s(x, t_k - \Delta t) - \Delta t \cdot v_n(x, s, t_k), \tag{18}$$

where $\boldsymbol{v} \cdot \widehat{\boldsymbol{n}}|_s$ was replaced with v_n. We assume that the ocean is hydrostatic and define p_w as the water pressure at the ice–water interface and p_w^0 as the hydrostatic water pressure. If l is sea level, the hydrostatic water pressure at k-th time step is governed by the following equation:

$$p_w^0(x, s, t_k) = \rho_w g(l(t_k) - s_*(x, t_k)). \tag{19}$$

3.3.3. Boundary conditions

Identifying $\widehat{\boldsymbol{n}}(\boldsymbol{x})$ as a unit outward normal vector at some point $\boldsymbol{x}$ of any domain boundary, we determine an orthogonal projection onto that boundary as a second-order tensor $\mathbb{P}$:

$$\mathbb{P} := \mathbb{I} - \widehat{\boldsymbol{n}}(\boldsymbol{x}) \otimes \widehat{\boldsymbol{n}}(\boldsymbol{x}), \tag{20}$$

where $\otimes$ is the tensor product. Denoting $\cdot$ as an inner product, we also define the projection of the Cauchy stress tensor $\boldsymbol{T}$ as

$$T_n = -\widehat{\boldsymbol{n}} \cdot \boldsymbol{T} \cdot \widehat{\boldsymbol{n}}. \tag{21}$$

Both models use the same Dirichlet boundary conditions provided in Table 2, where $v_0 > 0$ is the horizontal ice flow speed on the inflow boundary Γ_D.

Table 2. Models' boundary conditions

Boundary	Boundary condition	Physical meaning of a boundary condition	Equation number
Γ_w	$\boldsymbol{T} \cdot \widehat{\boldsymbol{n}} = -p_w \widehat{\boldsymbol{n}}$	Stress continuity at the ice–water boundary	(22)
Γ_a	$\boldsymbol{T} \cdot \widehat{\boldsymbol{n}} = 0$	No stress at the ice–air boundary	(23)

Γ_D	$\begin{cases} v_x = v_0 \\ \mathbb{P}T\hat{\boldsymbol{n}} = 0 \end{cases}$	On the inflow boundary the horizontal velocity is uniform and there is no vertical shear stress	(24)
Γ_N	$\boldsymbol{T} \cdot \hat{\boldsymbol{n}} = -\rho_i g(h-y)\hat{\boldsymbol{n}}$	Cryostatic normal-stress condition on the outflow boundary	(25)
Γ_b	$\mathbb{P}T\hat{\boldsymbol{n}} + \phi(\boldsymbol{v})\mathbb{P}\boldsymbol{v} = 0^*$	Sliding law on the ice-bed boundary	(26)
Γ_b	$\begin{cases} T_n \geq p_w \\ v_n \leq 0 \\ (T_n - p_w)v_n = 0 \end{cases}$	There are three possibilities for the normal stress and the normal velocity component on the ice-bed boundary: (1) The normal stress exceeds the water pressure ($T_n > p_w$) and the ice is not lifted off of the bed ($v_n = 0$); (2) The normal stress equals the water pressure ($T_n = p_w$) and the ice is lifted from the bed ($v_n < 0$); (3) The normal stress equals the water pressure ($T_n = p_w$), but the ice is not lifted from the bed ($v_n = 0$).	(27)
* in equation (26), $\phi(\boldsymbol{v}) = C(|\mathbb{P}\boldsymbol{v}|^2 + \varepsilon)^{\frac{1-n}{2n}}$ is friction with friction coefficient C and numerical parameter $\varepsilon \ll$ 1 (in $m^2 \cdot s^{-2}$) used to prevent numerical instabilities			

3.4. Viscoelastic model weak formulation

In this subsection, we provide the derivation of the viscoelastic model, while the viscous model is derived in Stubblefield et al. (2021). Let us define V as the velocity function space. K is a closed, convex subset of V such that

$$K = \left\{ \boldsymbol{v} \in V: \quad v_n|_{\Gamma_b} \leq 0 \quad and \quad v_x|_{\Gamma_D} = v_0 \right\} \tag{28}$$

Multiplying equation (7) by $\boldsymbol{v} - \boldsymbol{u}$ (where $\boldsymbol{u} \in K$ is an arbitrary test function), and integrating the expression over the glacier domain Ω, in the indicial notation we will get:

$$\int_\Omega (v_k - u_k)T_{kj,j}dV + \int_\Omega \rho_i g_k(v_k - u_k)dV = 0. \tag{29}$$

Integrating the first integral in equation (29) by parts and applying the divergence theorem (Green's identity), we then apply equation (11) to one of the integrals and rewrite the resulting expression in tensor notation:

$$-\int_{\partial\Omega} \boldsymbol{T} \cdot \hat{\boldsymbol{n}} \cdot (\boldsymbol{v} - \boldsymbol{u})da + \int_\Omega \{-p\nabla \cdot (\boldsymbol{v} - \boldsymbol{u}) + \boldsymbol{\tau} \cdot \nabla(\boldsymbol{v} - \boldsymbol{u}) - \rho_i g(\boldsymbol{v} - \boldsymbol{u})\}dV = 0. \tag{30}$$

Now, we decompose $\partial\Omega$ onto the compounding boundaries (see equation (2)) and consider the first integral in equation (30) over each boundary separately. Using equations (20), (21), and boundary condition (26) on Γ_b, after integration over Γ_b and taking into account that $T_n \geq p_w$ on Γ_b, we derive that

$$-\int_{\Gamma_b} \boldsymbol{T} \cdot \hat{\boldsymbol{n}} \cdot (\boldsymbol{v} - \boldsymbol{u})da \leq \int_{\Gamma_b} \alpha(\boldsymbol{v}) \cdot \mathbb{P}\boldsymbol{v} \cdot \mathbb{P}(\boldsymbol{v} - \boldsymbol{u})da + \int_{\Gamma_b} p_w(v_n - u_n)da. \tag{31}$$

On Γ_w, from equation (22), we obtain the following expression:

$$-\int_{\Gamma_w} \boldsymbol{T} \cdot \hat{\boldsymbol{n}} \cdot (\boldsymbol{v} - \boldsymbol{u})da = \int_{\Gamma_w} p_w(v_n - u_n)da. \tag{32}$$

284   On Γ_D, from equation (24), we have $\mathbb{P}T\hat{\boldsymbol{n}} = 0$, thus, this boundary does not contribute to the integral

285   $\int_{\partial\Omega} \boldsymbol{T} \cdot \hat{\boldsymbol{n}} \cdot (\boldsymbol{v} - \boldsymbol{u})da$. On Γ_a, from equation (23), we have $\boldsymbol{T} \cdot \hat{\boldsymbol{n}} = 0$, thus, this the ice-air boundary does not

286   contribute to the integral $\int_{\partial\Omega} \boldsymbol{T} \cdot \hat{\boldsymbol{n}} \cdot (\boldsymbol{v} - \boldsymbol{u})da$ as well. On Γ_N, where from equation (25), we know $\boldsymbol{T} \cdot \hat{\boldsymbol{n}} = -\rho_i g(h -$

287   $y)\hat{\boldsymbol{n}}$, which means that the contribution from the boundary to $\int_{\partial\Omega} \boldsymbol{T} \cdot \hat{\boldsymbol{n}} \cdot (\boldsymbol{v} - \boldsymbol{u})da$ will be

$$- \int_{\Gamma_N} \boldsymbol{T} \cdot \hat{\boldsymbol{n}} \cdot (\boldsymbol{v} - \boldsymbol{u})da = \int_{\Gamma_N} \rho_i g(h - y)(v_n - u_n)da. \tag{33}$$

288   Substituting equations (31) – (33) to equation (30), replacing the union of Γ_w and Γ_b with Γ_s and replacing p_w with

289   $p_w = \rho_w g(l - s + \Delta t \cdot v_n)$, which was derived from equations (18) and (19), we obtain

$$\int_\Omega \{-p\nabla \cdot (\boldsymbol{v} - \boldsymbol{u}) + \boldsymbol{\tau} \cdot \nabla(\boldsymbol{v} - \boldsymbol{u}) - \rho_i g(\boldsymbol{v} - \boldsymbol{u})\}dV + \int_{\Gamma_N} \rho_i g(h - y)(v_n - u_n)da +$$

$$+ \int_{\Gamma_b} \alpha(\boldsymbol{v}) \cdot \mathbb{P}\boldsymbol{v} \cdot \mathbb{P}(\boldsymbol{v} - \boldsymbol{u})da + \int_{\Gamma_s} \rho_w g(l - s + \Delta t \cdot v_n)(v_n - u_n)da \geq 0. \tag{34}$$

290   We define Q as a function space for pressure ($q \in Q$), and M as a function space for stress ($\mu \in M$). To shorten and

291   simplify the notation, we introduce following functions:

$$F(\boldsymbol{\tau}, \boldsymbol{v}, \boldsymbol{u}) = \int_\Omega \boldsymbol{\tau} \cdot \nabla\boldsymbol{u} - \rho_i g\boldsymbol{u}dV + \int_{\Gamma_N} \rho_i g(h - y)u_n da + \int_{\Gamma_b} \alpha(\boldsymbol{v}) \cdot \mathbb{P}\boldsymbol{v} \cdot \mathbb{P}\boldsymbol{u}da \tag{35}$$

$$P(\boldsymbol{v}, \boldsymbol{u}) = \int_{\Gamma_s} \rho_w g(l - s + \Delta t \cdot v_n)u_n da \tag{36}$$

$$d_\Omega(\boldsymbol{\mu}, \boldsymbol{\tau}, \boldsymbol{v}) = \int_\Omega \boldsymbol{\mu}\left(\tau + \frac{\eta}{G}\overset{\triangledown}{\tau} - 2\eta D(\boldsymbol{v})\right)dV \tag{37}$$

$$b_\Omega(q, \boldsymbol{v}) = \int_\Omega q\nabla \cdot \boldsymbol{v}dV \tag{38}$$

292   Writing inequality (34) in terms of equations (35) – (38), we obtain

$$\begin{cases} F(\boldsymbol{\tau}, \boldsymbol{v}, \boldsymbol{v} - \boldsymbol{u}) + P(\boldsymbol{v}, \boldsymbol{v} - \boldsymbol{u}) - b_\Omega(p, \boldsymbol{v} - \boldsymbol{u}) \geq 0 \\ d_\Omega(\boldsymbol{\mu}, \boldsymbol{\tau}, \boldsymbol{v}) = 0 \\ b_\Omega(q, \boldsymbol{v}) = 0 \end{cases}. \tag{39}$$

293   By analogy with Stubblefield et al. (2021) we replace the mixed formulation (39) with a penalty formulation

$$\begin{cases} F(\boldsymbol{\tau}, \boldsymbol{v}, \boldsymbol{u}) + P(\boldsymbol{v}, \boldsymbol{u}) - b_\Omega(p, \boldsymbol{u}) + \frac{\Pi'(\boldsymbol{v}, \boldsymbol{u})}{\epsilon} = 0 \\ d_\Omega(\boldsymbol{\mu}, \boldsymbol{\tau}, \boldsymbol{v}) = 0 \\ b_\Omega(\boldsymbol{q}, \boldsymbol{v}) = 0 \end{cases}. \tag{40}$$

294   Therefore, the penalized problem for the viscoelastic model is to find $(\boldsymbol{v}, p, \boldsymbol{\tau}) \in V \times Q \times M$, which satisfies the

295   boundary conditions and the system (40).

3.5.   Model setup

297   Both models consider a glacier as an incompressible, non-Newtonian ice flow, sharing the same domain and restricted

298   by identical boundary conditions. Using FEniCS, a freely available FEM Python package, both models employ

299   Taylor–Hood elements for velocity and pressure fields to solve the corresponding variational problem on each time

step by means of a Newton solver for nonlinear systems of equations. While Table S4 offers a brief comparison of the models, the primary distinction between the viscous and viscoelastic models lies in the incorporation of an elastic component, represented by Hooke's law. The addition of the elastic component enables the viscoelastic model to account for significant short-term glacier deformations, as provided by the application of the upper-convected Maxwell model of viscoelasticity. However, it also entails a substantial increase in computational resources required for a single model run (Table S4).

In the modeling framework, the bedrock slope is set using the function

$$b(x) = -\frac{Ax}{L},\tag{41}$$

where A is a variable parameter in meters that determines the bedrock inclination, and L is a glacier domain length, which is kept constant at 20 km for all model runs to ensure consistent results. The bed slope α is determined as the tangent of the bedrock function $b(x)$ and is measured

$$\alpha = \frac{A \cdot 100\%}{L}.\tag{42}$$

The grounding line position is defined based on the numerical tolerance ξ, set to 1 mm. If the computed position of a lower boundary mesh node s is ξ mm greater in the vertical direction than the bedrock, that node is classified as floating. Conversely, if a node position does not deviate from the bed by more than ξ, that node is classified as grounded. Schematically, the node classification can be described as:

$$\begin{cases} s - b \leq \xi \implies \text{grounded node} \\ s - b > \xi \implies \text{floating node} \end{cases}.\tag{43}$$

Both viscous and viscoelastic models require bed slope, glacier thickness and ice inflow speed as input parameters. For one set of input parameters, the code solves the corresponding variational problem twice: first, for a calm ocean surface without tides to stabilize the glacier and approximate its shape to a more natural geometry than the initially specified one; and second, for the tidal situation where the grounding zone width is determined. As follows from the CATS2008 model (Padman et al., 2002), the investigated glaciers experience tidal fluctuations with an amplitude of approximately 1 m. Therefore, in the model, we employ sinusoidal-shaped tides with a 1 m amplitude, and a half-day period P, which is typical for the investigated glaciers (Hibbins et al., 2010; Padman et al., 2018). Thus, the sea level, in a tidal case, changes with time as

$$l(t) = \frac{\rho_i}{\rho_w} H + sin\left(\frac{2\pi t}{P}\right),\tag{44}$$

where H is the glacier thickness at the grounding line. However, although the glaciers exhibit tidal fluctuations with a 1 m amplitude (or 2 m peak-to-peak amplitude), the DInSAR interferograms used for model accuracy assessment show only ~1 m peak-to-peak amplitude (Column ΔH in Table S6) due to the timing of the SAR image acquisition. To ensure a meaningful comparison between the measurements and the model results, the modeled grounding zones were calculated as the difference between grounding line positions sampled at the tidal levels corresponding to those captured by the DInSAR interferograms (Column H in Table S6).

We analyze the sensitivity of the models to mesh size by running simulations with the same set of parameters, while varying the mesh size at the lower domain surface (from 10 m to 250 m with 10 m step) and keeping the upper domain mesh fixed at 250 m. To determine the most efficient mesh size, 200 grounding zone width values were obtained and

331   analyzed (Figure S2). The accuracy of the viscoelastic model is more affected by mesh size than that of the viscous

332   model (see section 'S2. Mesh sensitivity analysis' in Supplementary materials). Since the empirically determined

333   manual grounding line mapping error can reach up to 200 m (Rignot et al., 2014; Ross et al., 2024), we conclude that

334   the mesh size impact remains within the confidence interval of manual mapping if the model outputs deviate by no

335   more than 0.2 km from the asymptotic value of the grounding zone width. Significant accuracy deterioration,

336   exceeding 200 m, occurs at a mesh size of 210 m for the viscous model (Figure S2 (a)) and 200 m for the viscoelastic

337   model (Figure S2 (d)). However, in the viscoelastic model, we observe several step-like changes in grounding zone

338   width, with the first noticeable shift occurring at a mesh size of 60 m (Figure S2 (b)). Therefore, to ensure the greatest

339   possible modelling precision and maintain the consistency of the results, we chose a 50 m mesh size at the lower

340   domain boundary for the following main analysis.

341   Model inputs were determined according to the MOS, TOT, and REN glaciers characteristics (Table S1 and

342   Figure S4). A total of 192 sets of initial parameters were investigated for each model, covering all possible

343   combinations of the ice thickness, ice inflow speed, and bedrock slope values listed in Figure S3. For each parameter

344   set, both the viscous and viscoelastic models were initially run for a duration of two months within the model's time

345   frame, assuming a stationary ocean with no tides to allow the model to reach stability. Subsequently, the models were

346   run over a 7-day period with tides incorporated. Since the models utilize sinusoidal waves for tide simulation, the still

347   water scenario corresponds to the zero-tide situation in the tidal problem. To justify these parameters we run multiple

348   tests, ensuring that the grounding zone width does not change whether a zero-tide, high-tide (+1 m), or low-tide (-

349   1 m) was chosen to initiate the tidal model run. The choice of a one-week time limit for the tidal problem allows the

350   model to adapt to tidal impacts. In most tidal model simulations, the grounding zone width slightly increases within

351   the first 3 to 5 days with each tide while the models adapt and stabilize afterward. Several test runs, lasting up to 14

352   days within the modeling framework, were conducted to estimate the impact of the grounding zone width increase

353   during the initial days. These test runs show that the grounding zone width stops changing after the first five days and

354   remains stable, showing no significant variations afterward. The initial increase occurs gradually, with the initial

355   grounding zone width being, on average, 80% of the final stabilized width, which is reached after 5 days. Therefore,

356   the resulting grounding zone width value for each model run is determined as the average of the grounding zone width

357   values simulated for days six and seven.

358   The source code of the viscous model, developed by Stubblefield et al. (2021), was used as a basis of the viscoelastic

359   model (see Code and Data availability). Necessary adjustments to the mesh size and glacier parameters for both

360   publicly available source codes were made accordingly. Consequently, a total of 1,168 model runs were performed

361   while conducting the research: 400 runs for the mesh sensitivity analysis and 768 runs for the main analysis, which

362   includes the grounding zone width dependence analysis from the main glacier parameters for both models. As for the

363   grounding line generation two model runs are required, 584 grounding zone values were obtained: 200 for the mesh

364   sensitivity analysis and 384 for the main analysis. In total, these code runs required about 1400 hours (~58 days) of

365   continuous computations.

4. Results

4.1. Measured glacier parameters

A summary of the glacier parameters, including ice flow speed, ice thickness, bed slope and grounding zone width, measured along the 69 selected profiles, is provided in Table S1. TOT exhibits the shallowest average bed slope among the glaciers of interest, measuring 1.2 ± 0.1 % on average. The glacier has an average grounding zone width of 4.1 ± 0.4 km and a mean thickness of 2.2 ± 0.1 km, making it the fastest among the three glaciers with an average speed of 647 ± 77 m/year. In contrast, REN is the thinnest and slowest among the three, with a mean thickness of 1.1 ± 0.2 km and a flow speed of 172 ± 24 m/year. It also features the smallest average grounding zone width of 2.3 ± 0.4 km and a rising inland bed with an average rate of 1.1 ± 0.2 %. MU, characterized by the smallest mean grounding zone of 2.1 ± 0.4 km, also has the steepest average bed slope of 2.2 ± 0.2 %. With an average thickness of 2.2 ± 0.1 km, the glacier maintains a mean ice flow speed of 335 ± 20 %.

The DInSAR-derived grounding zones exhibit an inverse relationship with bedrock slopes (Figure S1): larger grounding zones correspond to shallower slopes, while narrower grounding zones are found over steeper slopes. The correlation between bed slope (α) and grounding zone width (GZ), both for each glacier individually and for all three glaciers combined, can be modeled by an inverse power law function $\alpha = a \cdot GZ^b + c$, where the term 'inverse' indicates that the fitting coefficient b is negative. Based on the standard error of regression, we conclude that REN and TOT closely follow this inverse power law pattern, while MU introduces some variability, particularly due to its wide grounding zones exceeding 6 km. The standard error of 0.4 km, calculated when considering all three glaciers together, suggests that the overall relationship between grounding zone width and bedrock slope aligns well with the inverse power law model.

Additionally, Li et al. (2023) mentions that both ICESat laser altimetry and Sentinel-1a/b three-image DInSAR interferometry failed to delineate main trunk of TOT glacier and the central part of the MU main trunk due to the fast ice flow in these regions. On the contrary, the four-image CSK DInSAR technique utilized in this study allowed us to map grounding lines even over these fast-flowing areas. Li et al. (2023) estimated the average grounding line retreat between 1996 and 2020 as 3.51 ± 0.49 km for the southern lobe of the TOT main trunk, and as 13.85 km and 9.37 km for the western and eastern flanks of the MU main trunk, respectively. According to Li et al. (2023), it is impossible to determine the magnitude of tidally induced grounding line migrations in 1996 from the historic grounding line dataset (Rignot et al., 2016). Here we assume the 1996 grounding line position as the average position between high and low tides. To calculate the long-term retreat, we estimate the distance from the historic grounding line to the center of the DInSAR-derived grounding zones for each glacier of interest. As a result, for MU, between 1996 and 2021, we detect an average retreat of the main trunk of 9 ± 2 km, with 18 ± 1 km retreat at the western flank, 6.7 ± 0.6 km retreat at the central part of the main trunk, and 4.2 ± 0.6 km retreat at the eastern flunk. Thus, the western flank demonstrates the highest retreat rate of 690 ± 40 m/year, while the average glacier retreat rate over this period was 340 ± 80 m/year. For TOT, between 1996 and 2020, we observe an average retreat of the main trunk of 9 ± 3 km with 13.9 ± 0.1 km retreat at the western flank, 17 ± 1 km retreat at the central part of the main trunk, and 5.2 ± 0.3 km retreat at the eastern flank. Therefore, while the average rate of TOT retreat between 1996 and 2020 was 360 ± 120 m/year, the

central part of the main trunk retreated as fast as 680 ± 40 m/year. Meanwhile, the position of the REN grounding line at the main trunk did not change between 2000 and 2020, which indicates the stability of the glacier over the past 20 years.

4.2. Modeled Glaciers Parameters

4.2.1. The role of glacier thickness

Figure 5 shows the modeled grounding zone widths as a function of ice thickness, grouped by the bedrock slope and color-coded based on inflow speed. In both the viscous and viscoelastic models, the grounding zone width (GZ) exhibits a linear relationship with glacier thickness (H). Using the modeled grounding zone width values and approximating them with a linear function $GZ = a \cdot H + b$, we estimate coefficients of determination (R^2 values). Table S2 shows that R^2 ranges from 0.90 to 1.00 for the viscous model and from 0.87 to 1.00 for the viscoelastic model, which highlights a high linearity of the grounding zone dependence on the glacier thickness for all bedrock slopes. The main difference between the two models lies in the magnitude of the modeled grounding zone width as a function of glacier thickness over varying bed slopes. For example, for a bed slope of 0.05% and a glacier velocity of 800 m/yr, the viscous model predicts a grounding zone width of approximately 16 km, which is about twice the width estimated by the viscoelastic model (Figure 5).

In both models, shallower bed slopes increase the sensitivity of grounding zone width to changes in glacier thickness (Table S3). However, the viscous model is more sensitive to ice thickening compared to the viscoelastic model. In the viscous model, for slopes between 1.0% and 5.0%, the grounding zone width increases by less than 1 km as glacier thickness increases from 1 km to 2.5 km. In contrast, on a 0.05% bed slope, the grounding zone expands by 6.1 km due to the same increase in glacier thickness. The viscoelastic model, however, predicts a more moderate increase: for a 0.05% bed slope, ice thickening from 1 km to 2.5 km results in a 2.5 km widening of the grounding zone (Table S3). Thus, the viscous model predicts a more pronounced response to changes in bed slope compared to the viscoelastic model.

4.2.2. Influence of glacier velocity on grounding zone width

Our simulations enable us to characterize the behavior of the grounding zone width as a function of varying glacier velocities. Both models indicate that for slopes between 0.5% and 5.0%, an increase in ice inflow speed by 700 m/year results in up to a 10% expansion in grounding zone width (Figure 5). The most pronounced effect of velocity changes on grounding zone width occurs at shallower slopes of 0.1% and 0.05%. For these slopes, an increase in ice velocity from 100 m/year to 800 m/year can result in up to a 60% increase in grounding zone width in both the viscous and viscoelastic models (Figure 5). Additionally, both models show that at shallow slopes, glaciers with higher flow velocities are characterized by larger grounding zones for the same ice thickness. This indicates that for nearly flat bedrocks, a grounding zone width is more affected by variations in ice thickness for faster-flowing glaciers.
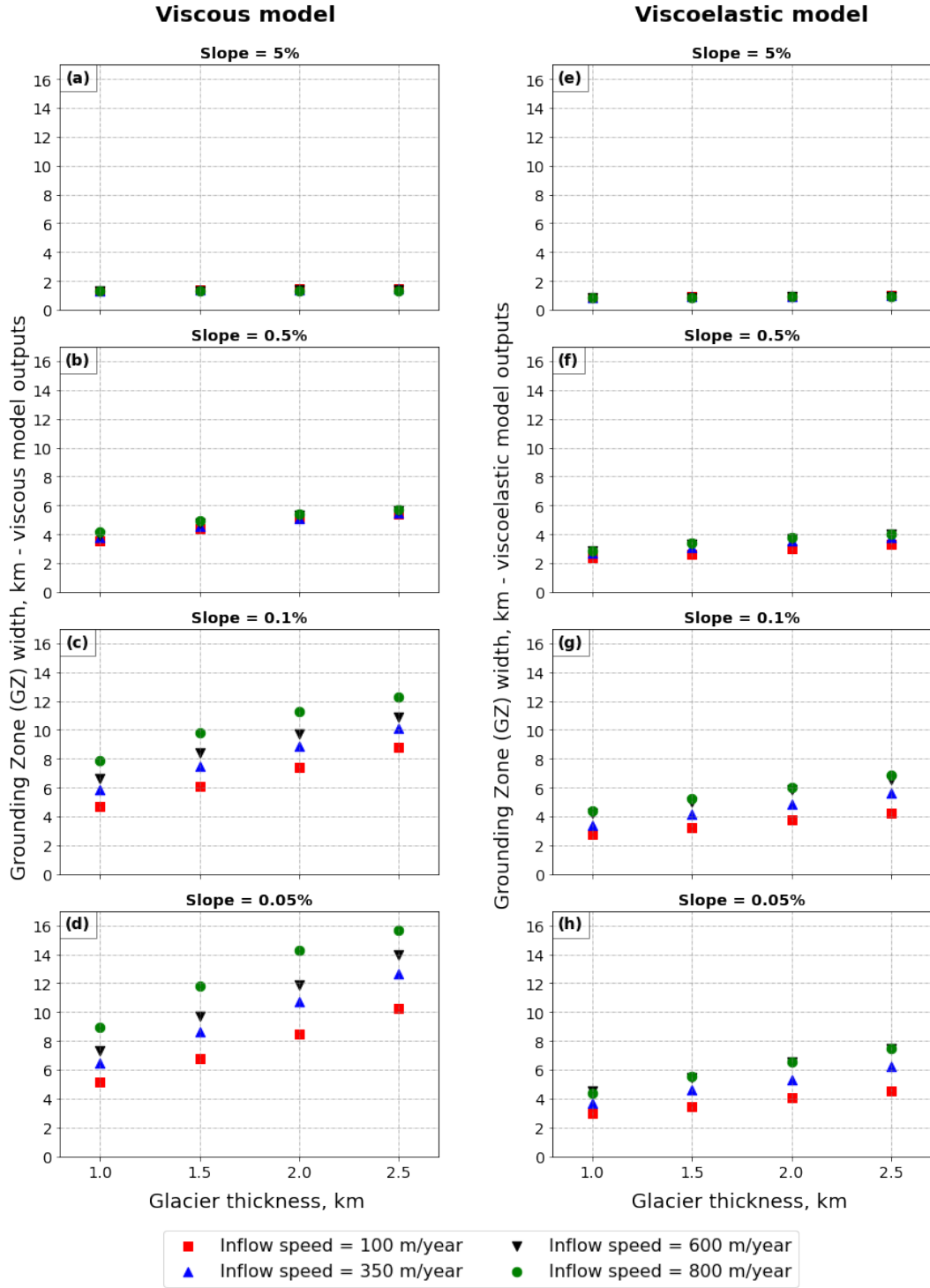
Figure 5. Dependence of the grounding zone width from the glacier thickness for inflow speeds of 100, 350, 600, and 800 m/year and bed slopes of 5, 0.5, 0.1, and 0.05% for both viscous (subplots (a) – (d)) and viscoelastic models (subplots (e) – (h)). Corresponding bed slope is written above each subplot, the x-axis of each subplot shows the glacier thickness in km, while the y-axis shows the evolution of the grounding zone as the glacier becomes thicker. Each subplot contains four sets of values, colored based on the model inflow speed.

4.2.3. Impact of bed slope on grounding zone extent

Figure 6 (a) and Figure 6 (b) present the grounding zone width obtained for the viscous and viscoelastic models, respectively, where the results for different inflow speeds are averaged by glacier thickness. Horizontal lines associated with the modeled grounding zones, in Figure 6 (a) and Figure 6 (b), represent the range of modeled grounding zone width values as a function of ice speed for a given ice thickness. In both models, grounding zone width increases as the bedrock slope decreases, indicating that the relationship between glacier bed slope and grounding zone width follows an inverse power law (dotted lines in Figure 6 (a) and (b)). The steepest rate of decay is observed for the thinnest glaciers (1 km), which are associated with the narrowest grounding zones. The shallowest power law applies to the thickest glaciers (2.5 km), resulting in the widest grounding zones.

The grounding zone width values from the viscoelastic model (GZ_{VE}) plotted against the outputs from the viscous model (GZ_V) reveal a linear relationship: $GZ_{VE} = 0.49 \cdot GZ_V + 0.47$, with a coefficient of determination (R^2) of 0.97 (Figure 6 (d)). Consequently, for any combination of bedrock slope, glacier thickness, and ice inflow speed, the grounding zone width obtained from the viscoelastic model is nearly half that of the grounding zone width calculated by the viscous model on shorter time scales.

4.3. Evaluation of model performance using DInSAR grounding zone measurements

Figure 6 (c) shows the superimposed outputs of the viscous and viscoelastic models alongside the DInSAR grounding zone measurements over MU, TOT, and REN glaciers overlaid on the outputs of both viscous and viscoelastic models. The dashed lines, outlining the models' domains, are shown in Figure 6 (a), (b), and (c), while their equations are provided in Figure 6 (a) and (b) with the corresponding standard error of regression (S). The models' domains, shown in Figure 6 (c) in pink for the viscous model and in green for the viscoelastic model, were determined using the function $\alpha = a \cdot GZ^b + c$, where α is the input bed slope, GZ is the modeled grounding zone, and a, b, and c are the fitting coefficients obtained through least-squares fit of the model outputs in Figure 6 (a) and (b). For each model, the upper domain boundary was established by fitting the largest modeled grounding zone outputs for each slope, while the lower domain boundary was defined by fitting the smallest modeled grounding zone outputs for each slope. The standard error of regression (S) is 0.12 and 0.16 for the upper and lower viscous domain boundaries, respectively, and 0.08 and 0.07 for the upper and lower viscoelastic domain boundaries, respectively. Therefore, the power law function $\alpha = a \cdot GZ^b + c$ accurately represents not only the DInSAR-derived grounding zone measurements (Figure S1), but also the models' output ranges.

To determine the models' accuracy, we measure the percentage of DInSAR measurements that fall inside the domain of a corresponding model. Disregarding the measurements error bars, only ~29%, ~0%, and ~9% of TOT's, REN's, and MU's measurements, respectively, fall into the viscous model's domain. Meanwhile, ~88% of TOT, 90% of REN, and ~82% of MU measurements (not accounting for the measurements errors) are successfully accommodated by the viscoelastic model. When including measurement errors, the model performance improves (Table S5). For the viscous model, the percentage of successfully modeled measurements increases from ~29% to ~65% for TOT, from ~0% to ~47% for REN, and from ~9% to ~82% for MU. For the viscoelastic model, this performance improvement is evident in the following notable expansions: from ~90% to ~100% for REN, from ~82% to ~100% for MU and remains consistently at ~88% for TOT. Overall, considering all three glaciers and all profiles, the viscous model achieves

approximately 12% accuracy without measurement error bars and 70% accuracy with them, while the viscoelastic model achieves around 86% accuracy without error bars and 97% accuracy with them. Therefore, considering all the profiles and the measurement error bars, the viscoelastic model outperforms the viscous model by ~28%. However, without error bars, the viscoelastic model outperforms the viscous model by ~74%. This finding underscores the critical importance of incorporating the elastic component in Navier-Stokes-based fluid glacier formulations for representing tidally induced grounding zone migrations.
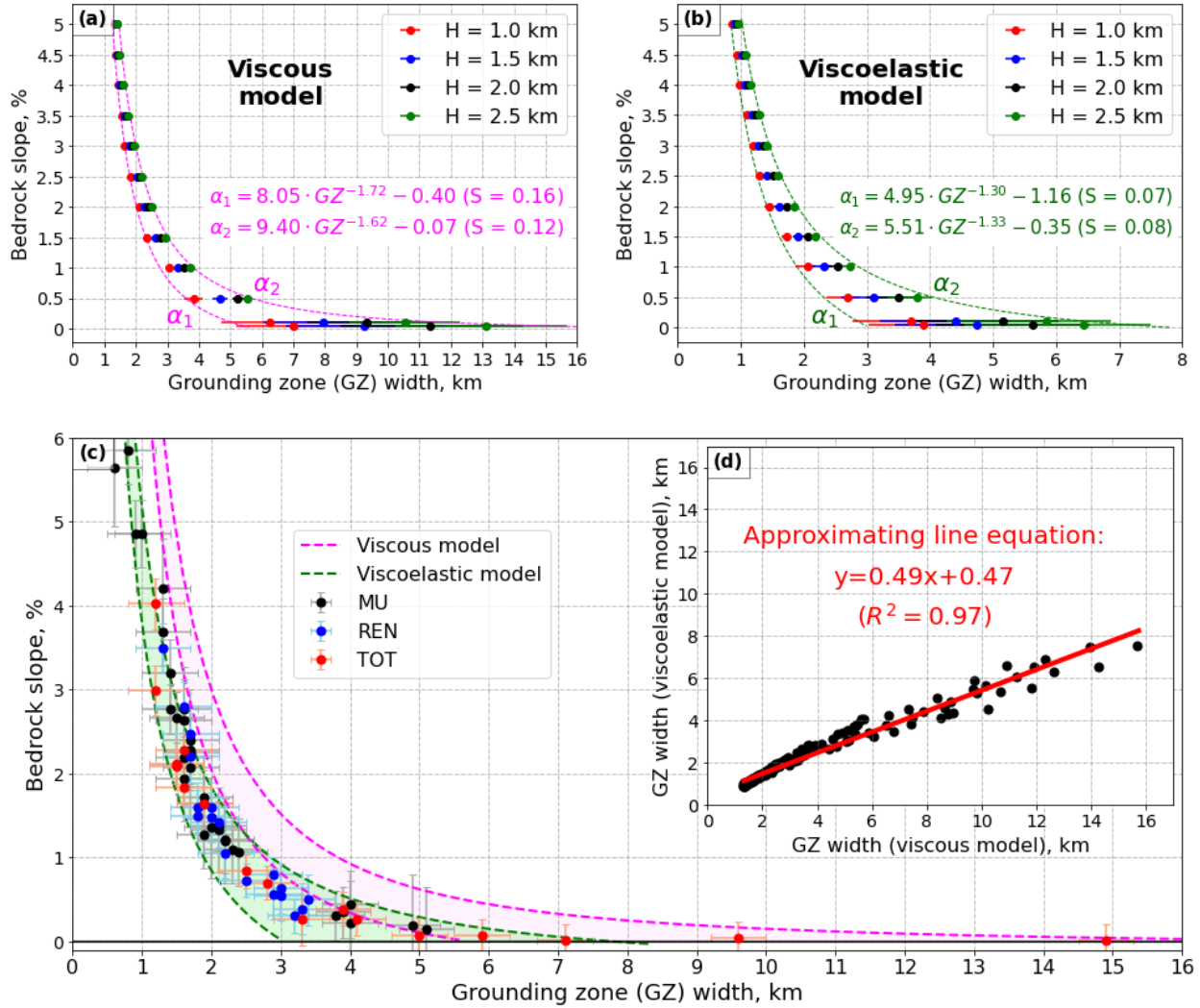
Figure 6. Modeling results of (a) viscous and (b) viscoelastic models, averaged by the thickness values, with pink and green outlines corresponding to maximum/minimum grounding zone (GZ) values for the same thickness but different inflow speeds; (c) comparison of the modelling results (pink and green areas) with the DInSAR grounding zone measurements; (d) correlation plot of the modelling results. Dotted green and pink lines are the same on subplots (a), (b), and (c), while their equations are provided in subplots (a) and (b).

5. Discussion

5.1. Grounding zone width dependence as a function of input parameters

Our models show that the grounding zone widens as the bed slope becomes shallower, following a non-linear relationship. This model-derived finding is consistent with our data as well as with previous observational studies (Chen et al., 2023; Milillo et al., 2017, 2019, 2022). Furthermore, both our models and data indicate that wider grounding zones are found where glaciers are thicker, with a linear relationship observed (Figure 7 (a) and (b)). This observation can be associated with the increase of the flexural wavelength of ice when its thickness increases (Freer et al., 2023). For thicker ice, the same tidal amplitude affects a larger horizontal distance, leading to a broader grounding zone. This effect is more pronounced on shallow slopes, where the tidal amplitude influences a larger area. Glacier velocity significantly impacts grounding zone width for bed slopes below 0.1% due to the increase in elastic stresses with faster glacier flow (Christmann et al., 2021). As a result, the elastic stress of fast-flowing glaciers on shallow slopes is higher than that of slower-moving glaciers, making the former more sensitive to thickness changes and confirming our observations (Figure 7 (c)).
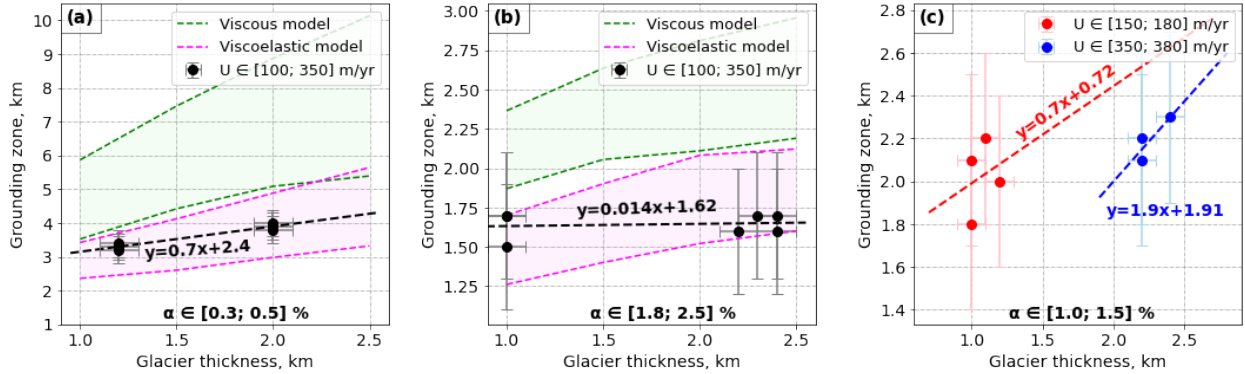
Figure 7. Relationship between glacier thickness and DInSAR-derived grounding zone width. (a) DInSAR measurements of grounding zone width (black dots) conducted along profiles characterized by bed slopes ranging from 0.3 to 0.5% and ice flow speeds from 100 to 350 m/year. The black dashed line shows the linear correlation between the ice thickness and DInSAR-derived grounding zones. (b) The black dots and the dashed line correspond to DInSAR measurements described by bed slopes ranging from 1.8 to 2.5% and ice flow speeds from 100 to 350 m/year, and their linear approximation, respectively. The green and pink areas in (a) and (b) correspond to the grounding zones, calculated by the viscous and viscoelastic models, respectively, for the same range of bed slopes and flow speeds as the DInSAR measurements, where pink and green dashed lines connect the corresponding model outputs. (c) Grounding zone measurements over 1.0 to 1.5% bed slopes, described by [150; 180] m/year and [350; 380] m/year ice flow speeds with corresponding linear approximations.

5.2. Role of elasticity

Using the viscous model for slopes not shallower than 2% can result in overestimating grounding zone widths by up to 25%. For slopes shallower than 2%, the viscous model overestimates grounding zone widths by up to 100% (Figure 6 (c)). The viscous model tends to overestimate the grounding zones compared to the viscoelastic model due to several

key factors. The viscoelastic model incorporates both the viscous (fluid-like) and elastic (solid-like) properties of ice, whereas the viscous model neglects the elastic component. This elastic response is fundamental over the tidal time scales, as ice exhibits elastic behavior under short-term deformations, such as those caused by tidal forces (Sayag and Worster, 2011; Warburton et al., 2020). Moreover, for cyclic loading, such as the tidal flexure of ice shelves, repeated loading and unloading make elastic effects significant (MacAyeal et al., 2015; Reeh et al., 2003). Additionally, the viscoelastic model more accurately captures time-dependent behavior by accounting for not only both the immediate elastic response and the delayed viscous response, but also the stress relaxation, a process neglected by purely viscous models (Christmann et al., 2019; MacAyeal et al., 2015). Research studies (Marsh et al., 2014; Reeh et al., 2000, 2003; Wild et al., 2017) confirm our conclusions regarding the critical importance of both viscous and elastic components at tidal timescales as viscoelastic models provide a more accurate representation of tidal bending processes.

While viscous models may be adequate for modeling long-term ice sheet evolution, they fail to represent important short-term phenomena such as tidal motion, seasonal cycles, and calving processes, which require the consideration of elastic responses. On the other hand, purely elastic models rely on a crucial simplification: they ignore the internal ice flow within the glacier, treating the glacier as a solid beam. Consequently, purely elastic models cannot realistically represent the complex nature of Antarctic glaciers, where the ice flow velocity in some glaciers exceeds 1 km/year (Rignot et al., 2011). By incorporating the viscous and elastic components in series, known as the Maxwell model of viscoelasticity, both slow and rapid deformations are considered. However, the simple Maxwell model describes small deformations, whereas the deformations of our interest may extend up to 50% of the glacier domain length. Therefore, we applied the upper-convected Maxwell model of viscoelasticity, which includes some geometrical non-linearity and allows the modeling of significantly larger deformations compared to the simple Maxwell model. Building on this, Christmann et al. (2021) emphasize that incorporating both viscous and elastic components is essential for realistic glacier dynamics modeling. In their study, the elastic component is crucial for accurately capturing the physical processes within a glacier, as it accounts for elastic strains in areas with sliding-dominated flow or high vertical deformations (Christmann et al., 2021). A similar argument was made by Hunke and Dukowicz (1997), highlighting that the elastic properties of ice temporarily reduce the overall deformation caused by the viscous component, which explains why the purely viscous model always estimates a wider grounding zone compared to the viscoelastic model. Elastic deformation is a short-term, recoverable response, while viscous deformation is a slower process that dominates over longer timescales. In situations involving short-duration forces, the elastic response can mitigate, but not eliminate, the visible effects of viscous deformation, providing a temporary reduction in overall glacier strain. This further highlights the necessity of incorporating both components for accurate modeling.

6. Conclusion

This study provides a comprehensive analysis of tide-induced grounding line variations across TOT, MU, and REN glaciers in East Antarctica, using both viscous and viscoelastic models. Our results emphasize the crucial role of ice elasticity in modeling grounding zone behavior, particularly for glaciers on shallow bed slopes. Given the 400 m uncertainty on DInSAR-based grounding zone width measurements, the viscoelastic model consistently outperforms the viscous model, capturing 97% of the grounding zone measurements when accounting for the measurement error.

Overall, both models can capture the rationally decaying relationship between grounding zone width (GZ) and bed slope (α), expressed as $\alpha = a \cdot GZ^b + c$, where a, b, and c are fitting parameters. The main difference lies in the dimensionless relaxation parameter b, which is ~24% smaller for the viscoelastic model, allowing it to better capture the observed dataset behavior. The elastic component introduces a damping effect, temporarily limiting the overall deformation caused by the viscous component (Hunke and Dukowicz, 1997). During a short timescale, the elastic component acts as a buffer, reducing the impact of elastic deformation, especially during cyclic events such as tidal flexure. This effect helps the viscoelastic model to accurately capture short-term glacier deformations and tidal-induced grounding zones. On average, the elastic component reduces the tidally induced grounding zone width by half, shielding the grounding zones from the infiltration of warm water that melts the glacier from below (Rignot et al., 2024), thereby promoting a stabilizing effect. Accounting for the DInSAR-derived grounding zone width measurements error, the viscous model may be applied for grounding zone widths of less than 1.5 km and slopes steeper than 3%. For shallower slopes, using a viscous model may lead to a 100% overestimation of the grounding zone width. These findings reinforce the need for incorporating both viscous and elastic components in short-term glacier models to improve the prediction of grounding zone dynamics.

Glacier thickness and velocity also influence the grounding zone width, with thicker glaciers and faster flow speeds contributing to wider grounding zones. Increased ice thickness extends the flexural wavelength, enlarging the area affected by tidal forces, while higher glacier velocities amplify elastic stresses, further expanding the grounding zone. These effects are especially pronounced on shallow bed slopes, where even small changes in thickness and velocity can lead to significant variations in grounding zone extent.

This research underscores the critical impact of glacier thickness, bed slope, and ice velocity on grounding zone width, with elastic stresses playing a key role in fast-flowing glaciers on shallow slopes. As climate change continues to influence polar regions, this modeling framework offers valuable insights for understanding and predicting grounding zone dynamics and their contributions to global sea level rise. Future research should focus on extending this model to include a broader range of glaciers and further refining the elastic-viscous model, particularly in response to tidal cycles and seasonal variations. This would enhance the model's predictive capability and provide deeper insights into how different environmental factors influence glacier dynamics, improving forecasts of grounding zone behavior and their implications for sea level rise.

Code and Data availability

All data needed to evaluate the conclusions in the paper are present in the paper and/or the Supplementary Materials. We thank the Italian Space Agency (ASI) for providing CSK data (original COSMO-SkyMed product ASI, Agenzia Spaziale Italiana (2008–2023)). Velocity (https://nsidc.org/data/NSIDC-0484/versions/2) and BedMachine (https://nsidc.org/data/NSIDC-0756/versions/2) data products are available at the National Snow and Ice Data Center, Boulder CO (NSIDC) website. The source codes for the viscous and viscoelastic models are freely available on https://github.com/agstub/grounding-line-methods/tree/v1.0.0 and https://github.com/agstub/viscoelastic-glines GitHub repositories, respectively. Geocoded interferograms and grounding-line positions are available at https://doi.org/10.5281/zenodo.10853336.

Author contribution

PM and NR designed the study; AS developed the viscous and viscoelastic models; NR performed the codes modifications and grounding zone simulations under the supervision of KN and RB; NR and PM performed the measurement of the grounding zones from the DInSAR data and the assessment of the main ice-bed system parameters; LD provided the CSK DInSAR data; NR and PM wrote the manuscript draft with contributions from KN, RB and AS reviewed and edited the manuscript. PM secured research funding.

Competing interests

The authors declare that they have no conflict of interest.

Acknowledgements

The research was conducted at the University of Houston, Houston, TX, US under a contract with the NASA's Cryosphere Program (NNH23ZDA001N-CRYO) and the Decadal Survey Incubation Program: Science and Technology (NNH21ZDA001N-DSI). We acknowledge the Research Computing Data Core (RCDC) for giving access to advance high-performance computing resources of the University of Houston. We extend our gratitude to the Italian Space Agency (ASI) for providing CSK data (original COSMO-SkyMed product ASI, Agenzia Spaziale Italiana (2008–2023)). We thank Konnor G. Ross for providing linguistic assistance during the peer-review process. We also thank the two anonymous reviewers for their valuable feedback, which greatly contributed to improving the quality of the manuscript.

References

Van Achter, G., Fichefet, T., Goosse, H., Pelletier, C., Sterlin, J., Huot, P.-V., Lemieux, J.-F., Fraser, A. D., Haubner, K., and Porter-Smith, R.: Modelling landfast sea ice and its influence on ocean–ice interactions in the area of the Totten Glacier, East Antarctica, Ocean Model (Oxf), 169, 101920, https://doi.org/10.1016/j.ocemod.2021.101920, 2022.

Aitken, A. R. A., Roberts, J. L., Ommen, T. D. van, Young, D. A., Golledge, N. R., Greenbaum, J. S., Blankenship, D. D., and Siegert, M. J.: Repeated large-scale retreat and advance of Totten Glacier indicated by inland bed erosion, Nature, 533, 385–389, https://doi.org/10.1038/nature17447, 2016.

Albrecht, N., Vennell, R., Williams, M., Stevens, C., Langhorne, P., Leonard, G., and Haskell, T.: Observation of sub-inertial internal tides in McMurdo Sound, Antarctica, Geophys Res Lett, 33, https://doi.org/10.1029/2006GL027377, 2006.

Allen, B., Mayewski, P. A., Lyons, W. B., and Spencer, M. J.: Glaciochemical Studies and Estimated Net Mass Balances for Rennick Glacier Area, Antarctica, Ann Glaciol, 7, 1–6, https://doi.org/10.3189/S0260305500005826, 1985.

Alnæs, M., Blechta, J., Hake, J., Johansson, A., Kehlet, B., Logg, A., Richardson, C., Ring, J., Rognes, M. E., and Wells, G. N.: The FEniCS project version 1.5, Archive of numerical software, 3, 2015.

622   Bensi, M., Kovačević, V., Donda, F., O'Brien, P. E., Armbrecht, L., and Armand, L. K.: Water masses distribution

623   offshore the Sabrina Coast (East Antarctica), Earth Syst Sci Data, 14, 65–78, https://doi.org/10.5194/essd-14-65-2022,

624   2022.

625   Brancato, V., Rignot, E., Milillo, P., Morlighem, M., Mouginot, J., An, L., Scheuchl, B., Jeong, S., Rizzoli, P.,

626   Bueso Bello, J. L., and Prats-Iraola, P.: Grounding Line Retreat of Denman Glacier, East Antarctica, Measured With

627   COSMO-SkyMed Radar Interferometry Data, Geophys Res Lett, 47, e2019GL086291,

628   https://doi.org/10.1029/2019GL086291, 2020.

629   Brunt, K. M., Fricker, H. A., Padman, L., Scambos, T. A., and O'Neel, S.: Mapping the grounding zone of the Ross

630   Ice Shelf, Antarctica, using ICESat laser altimetry, Ann Glaciol, 51, 71–79,

631   https://doi.org/10.3189/172756410791392790, 2010.

632   Chen, H., Rignot, E., Scheuchl, B., and Ehrenfeucht, S.: Grounding Zone of Amery Ice Shelf, Antarctica, From

633   Differential Synthetic-Aperture Radar Interferometry, Geophys Res Lett, 50, e2022GL102430,

634   https://doi.org/10.1029/2022GL102430, 2023.

635   Christmann, J., Muller, R., and Humbert, A.: On nonlinear strain theory for a viscoelastic material model and its

636   implications for calving of ice shelves, Journal of Glaciology, 65, 212–224, https://doi.org/10.1017/jog.2018.107,

637   2019.

638   Christmann, J., Helm, V., Khan, S. A., Kleiner, T., Müller, R., Morlighem, M., Neckel, N., Rückamp, M., Steinhage,

639   D., Zeising, O., and Humbert, A.: Elastic deformation plays a non-negligible role in Greenland's outlet glacier flow,

640   Commun Earth Environ, 2, 232, https://doi.org/10.1038/s43247-021-00296-3, 2021.

641   Coleman, R., Erofeeva, L., Fricker, H. A., Howard, S., and Padman, L.: A new tide model for the Antarctic ice shelves

642   and seas, Ann Glaciol, 34, 247–254, https://doi.org/DOI: 10.3189/172756402781817752, 2002.

643   Cornford, S. L., Seroussi, H., Asay-Davis, X. S., Gudmundsson, G. H., Arthern, R., Borstad, C., Christmann, J., Dias

644   dos Santos, T., Feldmann, J., Goldberg, D., Hoffman, M. J., Humbert, A., Kleiner, T., Leguy, G., Lipscomb, W. H.,

645   Merino, N., Durand, G., Morlighem, M., Pollard, D., Rückamp, M., Williams, C. R., and Yu, H.: Results of the third

646   Marine Ice Sheet Model Intercomparison Project (MISMIP+), Cryosphere, 14, 2283–2301, https://doi.org/10.5194/tc-

647   14-2283-2020, 2020.

648   Davison, B. J., Hogg, A. E., Rigby, R., Veldhuijsen, S., van Wessem, J. M., van den Broeke, M. R., Holland, P. R.,

649   Selley, H. L., and Dutrieux, P.: Sea level rise from West Antarctic mass loss significantly modified by large snowfall

650   anomalies, Nat Commun, 14, 1479, https://doi.org/10.1038/s41467-023-36990-3, 2023.

651   Dawson, G. J. and Bamber, J. L.: Antarctic Grounding Line Mapping From CryoSat-2 Radar Altimetry, Geophys Res

652   Lett, 44, 11,886-11,893, https://doi.org/10.1002/2017GL075589, 2017.

653   Durand, G., Gagliardini, O., de Fleurian, B., Zwinger, T., and Le Meur, E.: Marine ice sheet dynamics: Hysteresis and

654   neutral equilibrium, J Geophys Res, 114, F03009, https://doi.org/10.1029/2008JF001170, 2009.

655   Fernandez, R., Gulick, S., Domack, E., Montelli, A., Leventer, A., Shevenell, A., and Frederick, B.: Past ice stream

656   and ice sheet changes on the continental shelf off the Sabrina Coast, East Antarctica, Geomorphology, 317, 10–22,

657   https://doi.org/10.1016/j.geomorph.2018.05.020, 2018.

Freer, B. I. D., Marsh, O. J., Hogg, A. E., Fricker, H. A., and Padman, L.: Modes of Antarctic tidal grounding line migration revealed by Ice, Cloud, and land Elevation Satellite-2 (ICESat-2) laser altimetry, Cryosphere, 17, 4079–4101, https://doi.org/10.5194/tc-17-4079-2023, 2023.

Friedl, P., Weiser, F., Fluhrer, A., and Braun, M. H.: Remote sensing of glacier and ice sheet grounding lines: A review, Earth Sci Rev, 201, 102948, https://doi.org/10.1016/j.earscirev.2019.102948, 2020.

Gagliardini, O., Brondex, J., Gillet-Chaulet, F., Tavard, L., Peyaud, V., and Durand, G.: Brief communication: Impact of mesh resolution for MISMIP and MISMIP3d experiments using Elmer/Ice, Cryosphere, 10, 307–312, https://doi.org/10.5194/tc-10-307-2016, 2016.

Goldstein, R. M., Engelhardt, H., Kamb, B., and Frolich, R. M.: Satellite Radar Interferometry for Monitoring Ice Sheet Motion: Application to an Antarctic Ice Stream, Science (1979), 262, 1525–1530, https://doi.org/10.1126/science.262.5139.1525, 1993.

Gudmundsson, G. H.: Ice-stream response to ocean tides and the form of the basal sliding law, Cryosphere, 5, 259–270, https://doi.org/10.5194/tc-5-259-2011, 2011.

Haseloff, M. and Sergienko, O. V.: The effect of buttressing on grounding line dynamics, Journal of Glaciology, 64, 417–431, https://doi.org/10.1017/jog.2018.30, 2018.

Hersbach, H., Bell, B., Berrisford, P., Hirahara, S., Horányi, A., Muñoz-Sabater, J., Nicolas, J., Peubey, C., Radu, R., Schepers, D., Simmons, A., Soci, C., Abdalla, S., Abellan, X., Balsamo, G., Bechtold, P., Biavati, G., Bidlot, J., Bonavita, M., De Chiara, G., Dahlgren, P., Dee, D., Diamantakis, M., Dragani, R., Flemming, J., Forbes, R., Fuentes, M., Geer, A., Haimberger, L., Healy, S., Hogan, R. J., Hólm, E., Janisková, M., Keeley, S., Laloyaux, P., Lopez, P., Lupu, C., Radnoti, G., de Rosnay, P., Rozum, I., Vamborg, F., Villaume, S., and Thépaut, J.: The ERA5 global reanalysis, Quarterly Journal of the Royal Meteorological Society, 146, 1999–2049, https://doi.org/10.1002/qj.3803, 2020.

Hibbins, R. E., Marsh, O. J., McDonald, A. J., and Jarvis, M. J.: A new perspective on the longitudinal variability of the semidiurnal tide, Geophys Res Lett, 37, https://doi.org/10.1029/2010GL044015, 2010.

Holland, P. R.: A model of tidally dominated ocean processes near ice shelf grounding lines, J Geophys Res Oceans, 113, https://doi.org/10.1029/2007JC004576, 2008.

Hunke, E. C. and Dukowicz, J. K.: An Elastic–Viscous–Plastic Model for Sea Ice Dynamics, J Phys Oceanogr, 27, 1849–1867, https://doi.org/10.1175/1520-0485(1997)027<1849:AEVPMF>2.0.CO;2, 1997.

Li, T., Dawson, G. J., Chuter, S. J., and Bamber, J. L.: Grounding line retreat and tide-modulated ocean channels at Moscow University and Totten Glacier ice shelves, East Antarctica, Cryosphere, 17, 1003–1022, https://doi.org/10.5194/tc-17-1003-2023, 2023.

Logg, A., Mardal, K.-A., and Wells, G.: Automated solution of differential equations by the finite element method: The FEniCS book, Springer Science & Business Media, 2012.

Lowry, D. P., Han, H. K., Golledge, N. R., Gomez, N., Johnson, K. M., and McKay, R. M.: Ocean cavity regime shift reversed West Antarctic grounding line retreat in the late Holocene, Nat Commun, 15, 3176, https://doi.org/10.1038/s41467-024-47369-3, 2024.

MacAyeal, D. R., Sergienko, O. V, and Banwell, A. F.: A model of viscoelastic ice-shelf flexure, Journal of Glaciology, 61, 635–645, https://doi.org/DOI: 10.3189/2015JoG14J169, 2015.

Marsh, O. J., Rack, W., Golledge, N. R., Lawson, W., and Floricioiu, D.: Grounding-zone ice thickness from InSAR: Inverse modelling of tidal elastic bending, Journal of Glaciology, 60, 526–536, https://doi.org/DOI: 10.3189/2014JoG13J033, 2014.

Mayewski, P. A., Attig, J. W., and Drewry, D. J.: Pattern of Ice Surface Lowering for Rennick Glacier, Northern Victoria Land, Antarctica, Journal of Glaciology, 22, 53–65, https://doi.org/10.3189/S0022143000014052, 1979.

Meneghel, M., Bondesan, A., Salvatore, M. C., and Orombelli, G.: A model of the glacial retreat of upper Rennick Glacier, Victoria Land, Antarctica, Ann Glaciol, 29, 225–230, https://doi.org/10.3189/172756499781821463, 1999.

Miles, B. W. J., Stokes, C. R., Jamieson, S. S. R., Jordan, J. R., Gudmundsson, G. H., and Jenkins, A.: High spatial and temporal variability in Antarctic ice discharge linked to ice shelf buttressing and bed geometry, Sci Rep, 12, 10968, https://doi.org/10.1038/s41598-022-13517-2, 2022.

Milillo, P., Fielding, E. J., Shulz, W. H., Delbridge, B., and Burgmann, R.: COSMO-SkyMed Spotlight Interferometry Over Rural Areas: The Slumgullion Landslide in Colorado, USA, IEEE J Sel Top Appl Earth Obs Remote Sens, 7, 2919–2926, https://doi.org/10.1109/JSTARS.2014.2345664, 2014.

Milillo, P., Rignot, E., Mouginot, J., Scheuchl, B., Morlighem, M., Li, X., and Salzer, J. T.: On the Short-term Grounding Zone Dynamics of Pine Island Glacier, West Antarctica, Observed With COSMO-SkyMed Interferometric Data, Geophys Res Lett, 44, 10,436-10,444, https://doi.org/10.1002/2017GL074320, 2017.

Milillo, P., Rignot, E., Rizzoli, P., Scheuchl, B., Mouginot, J., Bueso-Bello, J., and Prats-Iraola, P.: Heterogeneous retreat and ice melt of Thwaites Glacier, West Antarctica, Sci Adv, 5, eaau3433, https://doi.org/10.1126/sciadv.aau3433, 2019.

Milillo, P., Rignot, E., Rizzoli, P., Scheuchl, B., Mouginot, J., Bueso-Bello, J. L., Prats-Iraola, P., and Dini, L.: Rapid glacier retreat rates observed in West Antarctica, Nat Geosci, 15, 48–53, https://doi.org/10.1038/s41561-021-00877-z, 2022.

Minchew, B. M., Simons, M., Riel, B., and Milillo, P.: Tidally induced variations in vertical and horizontal motion on Rutford Ice Stream, West Antarctica, inferred from remotely sensed observations, J Geophys Res Earth Surf, 122, 167–190, https://doi.org/10.1002/2016JF003971, 2017.

Mohajerani, Y., Velicogna, I., and Rignot, E.: Mass Loss of Totten and Moscow University Glaciers, East Antarctica, Using Regionally Optimized GRACE Mascons, Geophys Res Lett, 45, 7010–7018, https://doi.org/10.1029/2018GL078173, 2018.

Morlighem, M., Williams, C. N., Rignot, E., An, L., Arndt, J. E., Bamber, J. L., Catania, G., Chauché, N., Dowdeswell, J. A., Dorschel, B., Fenty, I., Hogan, K., Howat, I., Hubbard, A., Jakobsson, M., Jordan, T. M., Kjeldsen, K. K., Millan, R., Mayer, L., Mouginot, J., Noël, B. P. Y., O'Cofaigh, C., Palmer, S., Rysgaard, S., Seroussi, H., Siegert, M. J., Slabon, P., Straneo, F., van den Broeke, M. R., Weinrebe, W., Wood, M., and Zinglersen, K. B.: BedMachine v3: Complete Bed Topography and Ocean Bathymetry Mapping of Greenland From Multibeam Echo Sounding Combined With Mass Conservation, Geophys Res Lett, 44, 11–51, https://doi.org/10.1002/2017GL074954, 2017.

730 Orsi, A. H. and Webb, C. J.: Impact of Sea Ice Production off Sabrina Coast, East Antarctica, Geophys Res Lett, 49,

731 e2021GL095613, https://doi.org/10.1029/2021GL095613, 2022.

732 Padman, L., Fricker, H. A., Coleman, R., Howard, S., and Erofeeva, L.: A new tide model for the Antarctic ice shelves

733 and seas, Ann Glaciol, 34, 247–254, https://doi.org/10.3189/172756402781817752, 2002.

734 Padman, L., Siegfried, M. R., and Fricker, H. A.: Ocean Tide Influences on the Antarctic and Greenland Ice Sheets,

735 Reviews of Geophysics, 56, 142–184, https://doi.org/10.1002/2016RG000546, 2018.

736 Pritchard, H. D., Arthern, R. J., Vaughan, D. G., and Edwards, L. A.: Extensive dynamic thinning on the margins of

737 the Greenland and Antarctic ice sheets, Nature, 461, 971–975, https://doi.org/https://doi.org/10.1038/nature08471,

738 2009.

739 Pritchard, H. D., Ligtenberg, S. R. M., Fricker, H. A., Vaughan, D. G., van den Broeke, M. R., and Padman, L.:

740 Antarctic ice-sheet loss driven by basal melting of ice shelves, Nature, 484, 502–505,

741 https://doi.org/10.1038/nature10968, 2012.

742 Reeh, N., Mayer, C., Olesen, O. B., Christensen, E. L., and Thomsen, H. H.: Tidal movement of Nioghalvfjerdsfjorden

743 glacier, northeast Greenland: observations and modelling, Ann Glaciol, 31, 111–117, https://doi.org/DOI:

744 10.3189/172756400781820408, 2000.

745 Reeh, N., Christensen, E. L., Mayer, C., and Olesen, O. B.: Tidal bending of glaciers: a linear viscoelastic approach,

746 Ann Glaciol, 37, 83–89, https://doi.org/DOI: 10.3189/172756403781815663, 2003.

747 Rignot, E. and Thomas, R. H.: Mass Balance of Polar Ice Sheets, Science (1979), 297, 1502–1506,

748 https://doi.org/10.1126/science.1073888, 2002.

749 Rignot, E., Mouginot, J., and Scheuchl, B.: Ice flow of the Antarctic ice sheet, Science (1979), 333, 1427–1430, 2011.

750 Rignot, E., Jacobs, S., Mouginot, J., and Scheuchl, B.: Ice-Shelf Melting Around Antarctica, Science (1979), 341,

751 266–270, https://doi.org/10.1126/science.1235798, 2013.

752 Rignot, E., Mouginot, J., Morlighem, M., Seroussi, H., and Scheuchl, B.: Widespread, rapid grounding line retreat of

753 Pine Island, Thwaites, Smith, and Kohler glaciers, West Antarctica, from 1992 to 2011, Geophys Res Lett, 41, 3502–

754 3509, https://doi.org/10.1002/2014GL060140, 2014.

755 Rignot, E., Mouginot, J., and Scheuchl, B.: MEaSUREs Antarctic Grounding Line from Differential Satellite Radar

756 Interferometry, Version 2, Nat. Snow and Ice Data Center, https://doi.org/https://doi.org/10.5067/IKBWW4RYHF1Q,

757 2016.

758 Rignot, E., Mouginot, J., and Scheuchl, B.: MEaSUREs InSAR-based Antarctica ice velocity map, version 2, Nat.

759 Snow Ice Data Center, https://doi.org/https://doi.org/10.5067/D7GK8F5J8M8R, 2017.

760 Rignot, E., Mouginot, J., Scheuchl, B., van den Broeke, M., van Wessem, M. J., and Morlighem, M.: Four decades of

761 Antarctic Ice Sheet mass balance from 1979–2017, Proceedings of the National Academy of Sciences, 116, 1095–

762 1103, https://doi.org/10.1073/pnas.1812883116, 2019.

763 Rignot, E., Ciracì, E., Scheuchl, B., Tolpekin, V., Wollersheim, M., and Dow, C.: Widespread seawater intrusions

764 beneath the grounded ice of Thwaites Glacier, West Antarctica, Proceedings of the National Academy of Sciences,

765 121, e2404766121, https://doi.org/10.1073/pnas.2404766121, 2024.

766 Roberts, J., Galton-Fenzi, B. K., Paolo, F. S., Donnelly, C., Gwyther, D. E., Padman, L., Young, D., Warner, R.,

767 Greenbaum, J., Fricker, H. A., Payne, A. J., Cornford, S., Le Brocq, A., van Ommen, T., Blankenship, D., and Siegert,

768 M. J.: Ocean forced variability of Totten Glacier mass loss, Geological Society, London, Special Publications, 461,

769 175–186, https://doi.org/10.1144/SP461.6, 2018.

770 Rosier, S. H. R. and Gudmundsson, G. H.: Exploring mechanisms responsible for tidal modulation in flow of the

771 Filchner–Ronne Ice Shelf, Cryosphere, 14, 17–37, https://doi.org/10.5194/tc-14-17-2020, 2020.

772 Rosier, S. H. R., Gudmundsson, G. H., and Green, J. A. M.: Insights into ice stream dynamics through modelling their

773 response to tidal forcing, Cryosphere, 8, 1763–1775, https://doi.org/10.5194/tc-8-1763-2014, 2014.

774 Ross, N., Milillo, P., and Dini, L.: Automated grounding line delineation using deep learning and phase gradient-based

775 approaches   on   COSMO-SkyMed   DInSAR   data,   Remote   Sens   Environ,   315,   114429,

776 https://doi.org/https://doi.org/10.1016/j.rse.2024.114429, 2024.

777 Sayag, R. and Worster, M. G.: Elastic response of a grounded ice sheet coupled to a floating ice shelf, Phys Rev E,

778 84, 036111, https://doi.org/10.1103/PhysRevE.84.036111, 2011.

779 Schoof, C.: Ice sheet grounding line dynamics: Steady states, stability, and hysteresis, J Geophys Res, 112, F03S28,

780 https://doi.org/10.1029/2006JF000664, 2007.

781 Sergienko, O. and Haseloff, M.: 'Stable' and 'unstable' are not useful descriptions of marine ice sheets in the Earth's

782 climate system, Journal of Glaciology, 69, 1483–1499, https://doi.org/10.1017/jog.2023.40, 2023.

783 Sergienko, O. V: No general stability conditions for marine ice-sheet grounding lines in the presence of feedbacks,

784 Nat Commun, 13, 2265, https://doi.org/10.1038/s41467-022-29892-3, 2022.

785 Seroussi, H., Morlighem, M., Larour, E., Rignot, E., and Khazendar, A.: Hydrostatic grounding line parameterization

786 in ice sheet models, Cryosphere, 8, 2075–2087, https://doi.org/10.5194/tc-8-2075-2014, 2014.

787 Snoeijer, J. H., Pandey, A., Herrada, M. A., and Eggers, J.: The relationship between viscoelasticity and elasticity,

788 Proceedings of the Royal Society A: Mathematical, Physical and Engineering Sciences, 476, 20200419,

789 https://doi.org/10.1098/rspa.2020.0419, 2020.

790 Stubblefield, A. G., Spiegelman, M., and Creyts, T. T.: Variational formulation of marine ice-sheet and subglacial-

791 lake grounding-line dynamics, J Fluid Mech, 919, A23, https://doi.org/10.1017/jfm.2021.394, 2021.

792 Sturm, A. and Carryer, S. J.: Geology of the region between the Matusevich and Tucker Glaciers, north Victoria Land,

793 Antarctica,   New   Zealand   Journal   of   Geology   and   Geophysics,   13,   408–435,

794 https://doi.org/10.1080/00288306.1970.10423977, 1970.

795 Tsai, V. C. and Gudmundsson, G. H.: An improved model for tidally modulated grounding-line migration, Journal of

796 Glaciology, 61, 216–222, https://doi.org/10.3189/2015JoG14J152, 2015.

797 Warburton, K. L. P., Hewitt, D. R., and Neufeld, J. A.: Tidal Grounding-Line Migration Modulated by Subglacial

798 Hydrology, Geophys Res Lett, 47, e2020GL089088, https://doi.org/10.1029/2020GL089088, 2020.

799 Werner, C., Wegmüller, U., Strozzi, T., and Wiesmann, A.: Gamma SAR and interferometric processing software, in:

800 Proceedings of the ers-envisat symposium, Gothenburg, Sweden, 1620, 2000.

801 Wild, C. T., Marsh, O. J., and Rack, W.: Viscosity and elasticity: a model intercomparison of ice-shelf bending in an

802 Antarctic grounding zone, Journal of Glaciology, 63, 573–580, https://doi.org/DOI: 10.1017/jog.2017.15, 2017.